AGU PUBLICATIONS

JGR

Journal of Geophysical Research: Oceans

RESEARCH ARTICLE

10.1002/2014JC010474

Key Points:
- Underwater glider observes sediment transport in Hurricane Sandy
- Glider data are used to validate sediment transport modeling
- Model shows over 3 cm of erosion on the northern NJ shelf

Correspondence to:
T. Miles,
tnmiles@marine.rutgers.edu

Citation:
Miles, T., G. Seroka, J. Kohut, O. Schofield, and S. Glenn (2015), Glider observations and modeling of sediment transport in Hurricane Sandy, *J. Geophys. Res. Oceans*, *120*, 1771–1791, doi:10.1002/2014JC010474.

Received 26 SEP 2014
Accepted 2 FEB 2015
Accepted article online 6 FEB 2015
Published online 19 MAR 2015

This is an open access article under the terms of the Creative Commons Attribution-NonCommercial-NoDerivs License, which permits use and distribution in any medium, provided the original work is properly cited, the use is non-commercial and no modifications or adaptations are made.

Glider observations and modeling of sediment transport in Hurricane Sandy

Travis Miles[1], Greg Seroka[1], Josh Kohut[1], Oscar Schofield[1], and Scott Glenn[1]

[1]Center for Ocean Observing Leadership, Department of Marine and Coastal Sciences, School of Environmental and Biological Sciences, Rutgers University, New Brunswick, New Jersey, USA

Abstract Regional sediment resuspension and transport are examined as Hurricane Sandy made landfall on the Mid-Atlantic Bight (MAB) in October 2012. A Teledyne-Webb Slocum glider, equipped with a Nortek Aquadopp current profiler, was deployed on the continental shelf ahead of the storm, and is used to validate sediment transport routines coupled to the Regional Ocean Modeling System (ROMS). The glider was deployed on 25 October, 5 days before Sandy made landfall in southern New Jersey (NJ) and flew along the 40 m isobath south of the Hudson Shelf Valley. We used optical and acoustic backscatter to compare with two modeled size classes along the glider track, 0.1 and 0.4 mm sand, respectively. Observations and modeling revealed full water column resuspension for both size classes for over 24 h during peak waves and currents, with transport oriented along-shelf toward the southwest. Regional model predictions showed over 3 cm of sediment eroded on the northern portion of the NJ shelf where waves and currents were the highest. As the storm passed and winds reversed from onshore to offshore on the southern portion of the domain waves and subsequently orbital velocities necessary for resuspension were reduced leading to over 3 cm of deposition across the entire shelf, just north of Delaware Bay. This study highlights the utility of gliders as a new asset in support of the development and verification of regional sediment resuspension and transport models, particularly during large tropical and extratropical cyclones when in situ data sets are not readily available.

1. Introduction

At midnight on 29 October, Hurricane Sandy made landfall near Brigantine, NJ devastating New York and New Jersey coastal communities through a combination of high winds and historic storm surge [*Blake et al.*, 2013]. This storm caused significant coastal erosion [*Hapke et al.*, 2013], and showed a distinct seabed signature at an inner-shelf site [*Trembanis et al.*, 2013] but little is understood about broader regional sediment resuspension and transport on the continental shelf. A unique data set from a Teledyne-Webb Slocum glider equipped with a Nortek Aquadopp Current profiler deployed ahead of the storm in combination with the Regional Ocean Modeling System (ROMS) allow us to assess regional patterns of sediment resuspension and transport throughout Hurricane Sandy.

Storms are important episodic events that redistribute sediment on continental shelves [*Cacchione and Grant*, 1987; *Drake and Cacchione*, 1992; *Sherwood et al.*, 1994; *Ogston et al.*, 2000; *Keen and Glenn*, 2002; *Styles and Glenn*, 2005; *Teague et al.*, 2006; *Warner et al.*, 2008a]. Many of the field programs over the past two decades used benthic landers and tripods equipped with a suite of optical and acoustic sensors at a single location to understand sediment resuspension and transport dynamics [*Trowbridge and Nowell*, 1994; *Agrawal and Pottsmith*, 2000; *Harris et al.*, 2003; *Styles and Glenn*, 2005]. These sensor platforms have provided a wealth of information that have aided in the development of one-dimensional bottom boundary layer models (BBLMs) that take into account combined wave and current interactions [*Grant and Madsen*, 1979, 1986; *Glenn and Grant*, 1987; *Madsen and Wikramanayake*, 1991; *Madsen*, 1994; *Styles and Glenn*, 2000, 2002; *Warner et al.*, 2008b]. These one-dimensional models generally require input of wave and current data and a significant amount of tuning in order to accurately predict sediment resuspension and transport at a specific location.

In the past decade, these one-dimensional BBLMs have been coupled to three-dimensional hydrographic models to understand broader scale erosion and deposition at regional scales [*Blaas et al.*, 2007;

© 2015. The Authors.

Papanicolaou and Elhakeem, 2008; *Warner et al*., 2008b; *Hu et al*., 2009]. With the development of these regional scale sediment resuspension and transport studies new technologies are necessary to supplement single point measurements of sediment resuspension and transport on continental shelves. Many of the sensors included on tripods and benthic landers have now been developed for autonomous platforms such as Teledyne-Webb Slocum gliders [*Davis et al*., 2003; *Schofield et al*., 2007; *Glenn et al*., 2008]. A study by *Glenn et al*. [2008] presented data from two gliders deployed on the New Jersey shelf during storm conditions, one during stratified summer months and the other after the fall transition to well-mixed winter conditions. The stratified summer deployment showed sediment resuspension throughout the bottom layer, restricted by thermal stratification, during a summer hurricane, while the deployment after the fall transition identified full water column sediment resuspension that followed a Rousian distribution [*McLean*, 1991], where suspended sediment concentration decreased logarithmically with height above the bed. A follow up study [*Miles et al*., 2013] used two simultaneously deployed gliders during a northeaster in fall of 2009 to identify spatial variability in sediment resuspension and transport.

The present work builds on previous sediment resuspension and transport work by using a combination of model predictions and glider observations to identify idealized broad spatial patterns of sediment resuspension, transport, and deposition on the New Jersey (NJ) continental shelf during Hurricane Sandy in October of 2012.

A detailed description of observational and model setup is given in section 2. The synoptic atmospheric and oceanic conditions, as well as the observed and modeled sediment resuspension and transport response along the glider track are detailed in section 3. Section 4 provides a broader regional look at sediment transport throughout the storm and highlights the atmospheric and wave forcing that lead to shelf wide patterns of erosion and deposition. A final summary and conclusions are provided in section 5.

2. Methods

2.1. Gliders

Teledyne-Webb Slocum gliders have become robust tools for sampling storm conditions [*Glenn et al*., 2008; *Ruiz et al*., 2012; *Miles et al*., 2013]. These instruments are mobile sensor platforms that profile through the water column using a combination of buoyancy and a set pitch angle to move vertically and horizontally in a sawtooth pattern. Data are logged every 2 s on downcast and upcast with vertical speeds of $\sim$20 cm/s resulting in high data density relative to traditional shipboard techniques. A single hour long sampling segment may include approximately 5–10 profiles depending on water column depth. After each segment is complete the glider surfaces and relays its position and data back to Rutgers using an Iridium satellite phone in the aft section of the glider. Further details of Rutgers glider operations can be found in *Schofield et al*. [2007].

The glider used in this study was RU23, a first generation shallow (100 m rated) glider equipped with a suite of oceanographic sensors. RU23 included three science sensors, a Seabird unpumped conductivity temperature and depth (CTD) sensor, two Wetlabs triplet sensors and an externally mounted Nortek Aquadopp current profiler. One Wetlabs triplet was an optical backscatter puck (bb3) that measured the volume scattering function (VSF) at three wavelengths 470, 532, and 660 nm in the 117° back direction. We converted from the VSF to estimated backscatter coefficients following *Boss and Pegau* [2001]. For our analysis, we use the 660 nm channel as it is less impacted by absorption effects than the shorter wavelength channels (E. Boss, personal communication, 2014). These instruments respond linearly to increased suspended particulate matter concentrations [*Boss et al*., 2009], but are also sensitive to variability in particle size, shape, and composition; similar sensors were used onboard previous glider observations of storm driven sediment resuspension and transport [*Glenn et al*., 2008; *Miles et al*., 2013]. The second Wetlabs triplet was an ecopuck that we used primarily to measure chlorophyll fluorescence.

The Nortek Aquadopp was a three-beam 2 MHz system with a 0.2 m blanking distance that collected data in 10 1 m bins in beam coordinates. The Aquadopp was externally mounted in an upward looking position, with a custom glider head that measured 0° pitch at a nominal glider pitch angle of 26.5°. Data were logged internally and downloaded postdeployment. This instrument served two purposes: the first was to estimate realistic water column velocities following a shear least squares method originally developed for lowered

© 2015. The Authors.

acoustic Doppler current profilers [*Visbeck*, 2002] and recently adapted to use on glider platforms [*Todd et al*., 2011a, 2011b]. The shear least squared method is used to solve the following equation:

$$(u,v)_r = (u,v)_w - (u,v)_g \tag{1}$$

where $(u,v)_r$ is the measured water velocity relative to the glider, $(u,v)_w$ is the real ocean velocity, and $(u,v)_g$ is the velocity of the glider. The measured water velocity relative to the glider is taken directly from the vertical profile of the horizontal shear of the velocity profiles above the glider. Glider velocity is dead-reckoned [*Davis et al*., 2003] using a combination of pre and postsegment GPS fixes, pitch angle, heading, and depth. These two measurements are then used to solve for the real ocean velocities using least squares, which are described in detail in Appendix B of *Todd et al*. [2011a].

The second purpose was to provide acoustic backscatter observations coincident with optical measurements. Acoustic return (*Amp*) strength along each beam was converted to echo level (*EL*), with units of decibels (dB) following *Lohrmann* [2001]:

$$EL = Amp \times 0.43 + 20\log_{10}(R) + 2\alpha_w R + 20R\int \alpha_p \times dr \tag{2}$$

where R is the range along each beam, α_w is the water absorption in db m^{-1}, and α_p is the particle attenuation in db m^{-1}. Previous studies [e.g., *Lynch et al*., 1997] have used colocated optical and acoustic backscatter sensors on bottom tripods to assess the relative contribution of small and large sediment particles. The difference in acoustic and optical response to different size classes is most clearly illustrated in *Lynch et al*. [1997, Figure 4], with an optical backscatter sensor and a 1 and 5 MHz acoustic backscatter sensor. An Aquadopp is most sensitive to particles with a $k^*a = 1$, where k is the acoustic wave number and a is the particle radius [*Lohrmann*, 2001; *Thorne and Hanes*, 2002]. For a 2 MHz system, a k*a value is most sensitive to particles with a 0.25 mm diameter with a reduction in sensitivity raised to the fourth power for particles smaller than a and inversely proportional for particles with a diameter larger than a. Optical backscatter sensors generally respond to the cross-sectional area [*Bunt et al*., 1999] and have been shown to have large increases in observed optical backscatter for similar concentrations of small versus large particles, thus in the presence of significant concentrations of small suspended particles these sensors are largely unresponsive to additional concentrations of large particles (C. Sherwood, personal communication, 2014).

As the glider was deployed over a broad spatial region with varying bottom types, sediment types and optical properties we did not attempt to calibrate either optical or acoustic backscatter sensors using in situ sediment, but rather focus on intercomparison of the suite of sensors to estimate sediment resuspension and transport throughout the deployment.

2.2. Additional Observational Assets

We use National Oceanographic and Atmospheric Association (NOAA) buoy 44025 and 44009 data to supplement glider data and validate numerical model results. NOAA buoy 44025 is located at 40.250°N and 73.167°W off of Long Island, New York, and NOAA buoy 44009 is located at 38.461°N and 74.703°W offshore of Delaware Bay (Figure 1). Buoy data included in this study are hourly wind speed and direction collected at a height of 4 m, barometric pressure, significant wave height, dominant wave period, wave spectra, and mean wave direction from buoy 44025 only.

2.3. Hydrodynamic Model

The Regional Ocean Modeling System (ROMS) [*Shchepetkin and McWilliams*, 2005, 2009; *Haidvogel et al*., 2008] version 3.6 was used to simulate the ocean response to storm forcing. ROMS is a free surface, sigma coordinate primitive equation model that is widely used for coastal applications. The configuration here is a modified version of the Experimental System for Predicting Shelf and Slope Optics (ESPreSSO) (http://www.myroms.org/espresso/) with 5 km horizontal resolution and 36 vertical levels, which extends from Cape Cod, MA, to Cape Hatteras, NC, and near shore to beyond the shelf-break (Figure 2). The ESPreSSO domain has been used extensively on the MAB to study a diverse array of physical and biological processes [*Cahill et al*., 2008; *Haidvogel et al*., 2008; *Hofmann et al*., 2008; *Zhang et al*., 2009; *Wilkin and Hunter*, 2013; *Xu et al*., 2013]. We used the original assimilative ESPreSSO four-dimensional variational data assimilations (IS4DVAR) output as an initial condition starting on 25 October and ran the model forward including boundary

© 2015. The Authors.

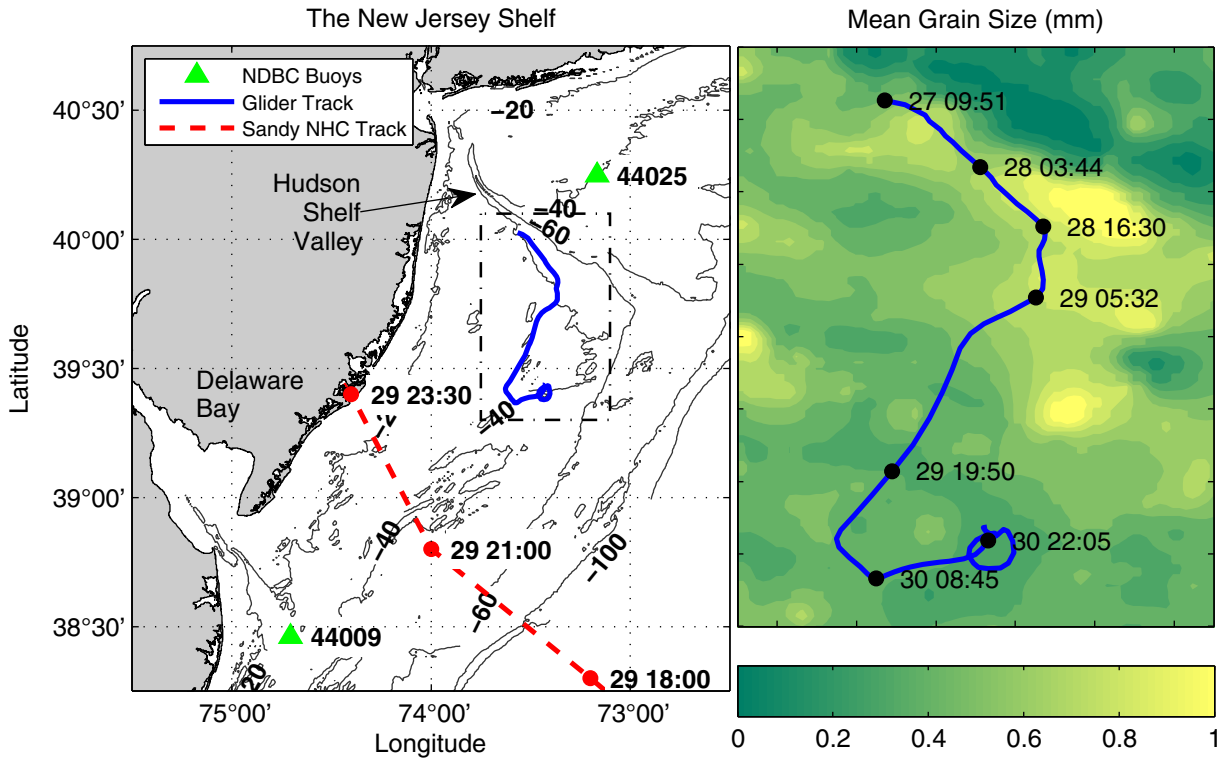

Figure 1. Map of the (a) New Jersey shelf, with locations of buoys (green diamonds) 44025 and 44009, (blue line) RU23 glider sampling track, the (red dashed line) Hurricane Sandy track from the National Hurricane Center (NHC) with associated time points. (b) A map of mean bed grain sizes over the area defined by the dashed box in Figure 1a in millimeters compiled from the usSEABED project, with a (blue line) track of the glider consistent with Figure 1a overlaid with times in the format of day hour:minute on 27 October through 30 October 2012.

conditions from HYCOM-NCODA (http://hycom.org/), tidal boundary conditions from the ADCIRC tidal model (http://adcirc.org/).

For this study, we modify the standard ESPreSSO setup in a number of ways: we replace the standard ESPreSSO atmospheric forcing from the National Center for Environmental Prediction (NCEP) North American Mesoscale (NAM) model with our own Weather Research and Forecasting (WRF) model detailed in section 2.4; by turning on the sediment features detailed in section 2.5; and the BBLM detailed in section 2.6; and drive this BBLM with the wave information from NOAAs, WAVEWATCH III model detailed in section 2.7. While numerous studies have used the Coupled Ocean Atmosphere Wave Sediment Transport (COAWST) system [*Warner et al.*, 2010; *Olabarrieta et al.*, 2012] for sediment transport, which includes a coupled wave and atmospheric model, for simplicity we use the Rutgers ROMS ESPreSSO domain as it has a robust history of reproducing realistic circulation over our study region [*Wilkin and Hunter*, 2013] and required minimal adjustment from the standard setup to run for the purposes of this study.

2.4. Atmospheric Model

Default atmospheric forcing for ROMS ESPreSSO is from the NCEP NAM model, which is an operational version of the WRF Nonhydrostatic Mesoscale Model (WRF-NMM) run at 12 km horizontal resolution with standard output every 3 h. In order to provide ROMS with higher spatial and temporal resolution atmospheric forcing, we used our own implementation of the Advanced Research WRF (WRF-ARW), Version 3.4 [*Skamarock et al.*, 2008]. WRF-ARW is a fully compressible, nonhydrostatic, terrain-following coordinate, primitive equation atmospheric model that is used for many different weather and climate applications.

Our WRF-ARW simulations were run at 6 km horizontal resolution with 35 vertical levels, using the Global Forecast System (GFS) 0.5° model for lateral boundary conditions. To provide continuous near-analysis atmospheric forcing, we used hourly output from a series of six short 36 h WRF-ARW hindcasts. These hindcasts were initialized at 00:00 GMT each day starting on 25 October 2012. For each run, excluding the first

 © 2015. The Authors.

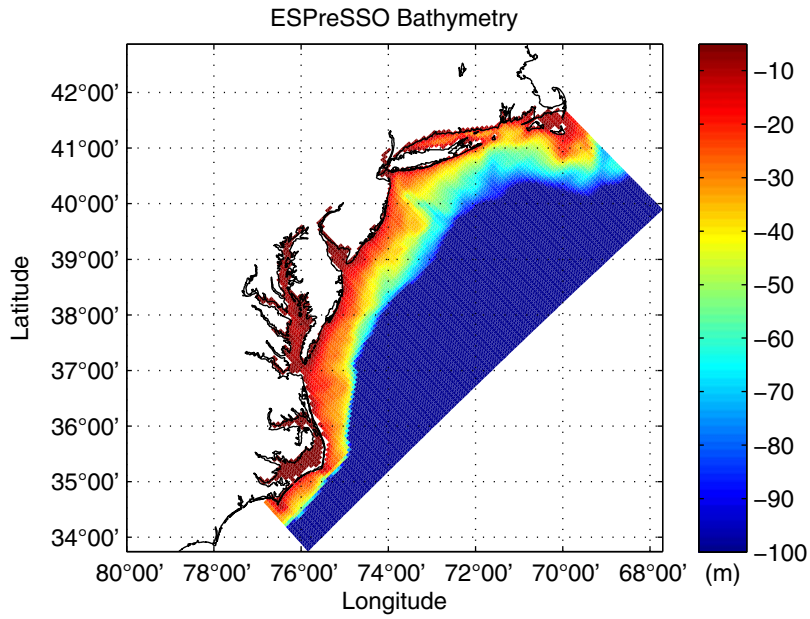

Figure 2. A map of bathymetry for the ESPreSSO model domain (gridded region) with the maximum plotted depth of 100 m. Depths beyond 100 m are present in the model domain but are plotted as blue here.

and last runs, only data from hours 7 to 30 were retained in an effort to minimize the impact of model reinitialization on wind forcing. The first run included hours 1 through 30 and the last run included hours 7 to 36 in an effort to maximize coverage.

For bottom boundary conditions over water, we used a high-resolution sea surface temperature (SST) composite product. This daily SST product has a resolution of 2 km and is a 3 day coldest dark pixel composite of regionally declouded daytime scans from the Advanced Very High Resolution Radiometer (AVHRR) aboard the NOAA-18 and NOAA-19 satellites. Through these techniques, normally unresolved coastal upwelling and tropical cyclone cold wake processes are preserved. For each simulation, we initialize SST with the daily composite described above and leave it fixed until the next simulation's initialization. Model validations in section 3.3 indicate that this model setup adequately represents storm forcing for our purposes, but future model runs may benefit from coupled ocean and atmospheric modeling.

ESPreSSO air-sea heat and momentum fluxes were calculated using the bulk formulae of *Fairall and Bradley* [1996] and *Fairall et al*. [2003] using the ESPreSSO model sea surface temperature and WRF-ARW sea level air temperature, precipitation, pressure, relative humidity, and 10 m winds.

2.5. Sediment Model

We used the Community Sediment Transport Model (CSTM) to simulate sediment resuspension and transport. A detailed description of the CSTM can be found in *Warner et al*. [2008b]. The CSTM requires input of user-defined sediment size classes, critical shear stress values, fall velocities, densities, and erodibility constants. We initialized with an idealized spatially uniform single, 15 m deep, bed layer with two noncohesive size classes of 0.1 mm and 0.4 mm to represent fine and medium grain size sands found in the glider sample region (Figure 1b). According to a map generated from data collected by the usSEABED project [*Goff et al*., 2008] on 29 October 2012 during peak storm conditions, the glider was sampling over a region with approximately 0.4 mm mean grain sizes. Additionally, a recent publication [*Trembanis et al*., 2013] collected grab samples on the southern region, near buoy 44009 and identified mean grain sizes of approximately 0.3 mm prior to Sandy impacting the region. Based on the 0.1 and 0.4 mm diameters and 2650 kg m^{-3} densities, we use settling velocities and critical shear stresses of 5.7 mm s^{-1} and 0.14 N m^{-2}, respectively, for the 0.1 mm sediment and 52 mm s^{-1} and 0.23 N m^{-2} for the 0.4 mm sediment and erodibility constants of 5×10^{-4} kg m^{-2} s^{-1} for both sediment types. This uniform bed setup is used to only generally represent sediment resuspension and transport on the continental shelf, and is primarily used for simplification of data interpretation and comparison of large and small grain size particles with glider data. This setup will

© 2015. The Authors.

not address the potential impact of realistic sediment distributions and bed armoring on sediment resuspension. For more detailed analysis, we recommend using a broader array of sediment types, higher spatial resolution model grids, and coupled ocean-atmosphere-wave model routines.

At each time step, the model uses sediment bed properties to calculate bed roughness at each grid point and passes this information to the bottom boundary layer model to calculate bottom stress (τ_{sf}) from combined waves and currents. If critical shear stresses (τ_{ce}) are exceeded sediment is resuspended into the water column and transported as a tracer similar to temperature and salinity, but with an additional source and sink term, based on the erosional source and settling velocity, respectively. From *Warner et al*. [2008b]:

$$C_{source,m} = \frac{\partial w_{s,m} C_m}{\partial s} + E_{s,m} \tag{3}$$

where s is the vertical coordinate for the advection diffusion equation in ROMS, w_s is the vertical settling velocity prescribed by the user for each size class m, C is sediment concentration, and E_s is the erosion source, which follows[*Ariathurai and Arulanandan*, 1978]:

$$E_{s,m} = E_{0,m}(1-\phi)\ \frac{\tau_{sf} - \tau_{ce,m}}{\tau_{ce,m}} \quad \tau_{sf} > \tau_{ce,m} \tag{4}$$

where again, s is the vertical coordinate in ROMS, E_s is the surface erosion mass flux, E_0 is a bed erodibility constant, ϕ is the bed porosity of the uppermost bed layer and τ_{sf} τ_{ce} are the defined above. For the purposes of this study, we only consider suspended load transport for direct comparison with glider observed suspended load transport, though for realistic studies of sediment transport bedload transport must be considered. Bedload transport routines are also available in ROMS [*Meyer-Peter and Müller*, 1948; *Soulsby and Damgaard*, 2005].

2.6. Bottom Boundary Layer Model

The standard ESPreSSO setup uses a quadratic drag law with a drag coefficient expression to represent bottom stress. For sediment resuspension and transport, a more detailed calculation of bottom stress is needed as realistically, large gradients in velocity and sediment concentration occur near the bed. For this study, we use the ssw_bbl model, which follows *Madsen* [1994] for combined waves and currents and the moveable bed routines from *Wiberg and Harris* [1994] and *Harris and Wiberg* [2002]. The ssw_bbl routine used in this study is covered in detail in *Warner et al*. [2008b]. Parameters required for the ssw_bbl model include sediment characteristics described in the previous section to determine bed roughness, near-bottom reference velocities, u and v taken as the velocity in the lowest model grid, wave orbital velocities u_b, wave period T, and wave direction θ.

2.7. Wave Model

The wave parameters used for this study are derived from the third generation NOAA WAVEWATCH III (WWIII) (http://polar.ncep.noaa.gov/waves/index2.shtml) operational wave model. We specifically use data from the hindcast reanalysis version 2.22, with 3 h output. We use two WWIII data sets for this study, with 4° and 10° min resolutions that cover the study region. The 4 min resolution data does not cover the entire ESPreSSO domain but provides higher resolution in near shore shallow water regions. Both the 4 and 10 min resolution data are interpolated to the standard ESPreSSO grid with a nominal 5 km horizontal resolution. While this may not be an ideal methodology for detailed analysis of coastal change or long-term studies on the continental shelf, interpolation of these readily available products were sufficient for a first-order comparison of glider optical data to modeled suspended sediment at the midshelf. WWIII model hindcasts do not include the full wave spectra as the operational and forward run products. To calculate bottom orbital velocities from WWIII data without spectral information, we use linear wave theory and follow the method of *Wiberg and Sherwood* [2008] using an assumed Joint North Sea Wave Project (JONSWAP) spectrum. Matlab® codes for this calculation are included in the reference and validation of the calculated product of both buoys is presented in section 3.3.

3. Results

3.1. Storm Conditions

On 28 October, when winds and waves began to steadily increase on the MAB (Figure 3) the center of Hurricane Sandy was located nearly due east of the Georgia and South Carolina. On 29 October, the storm began

© 2015. The Authors.

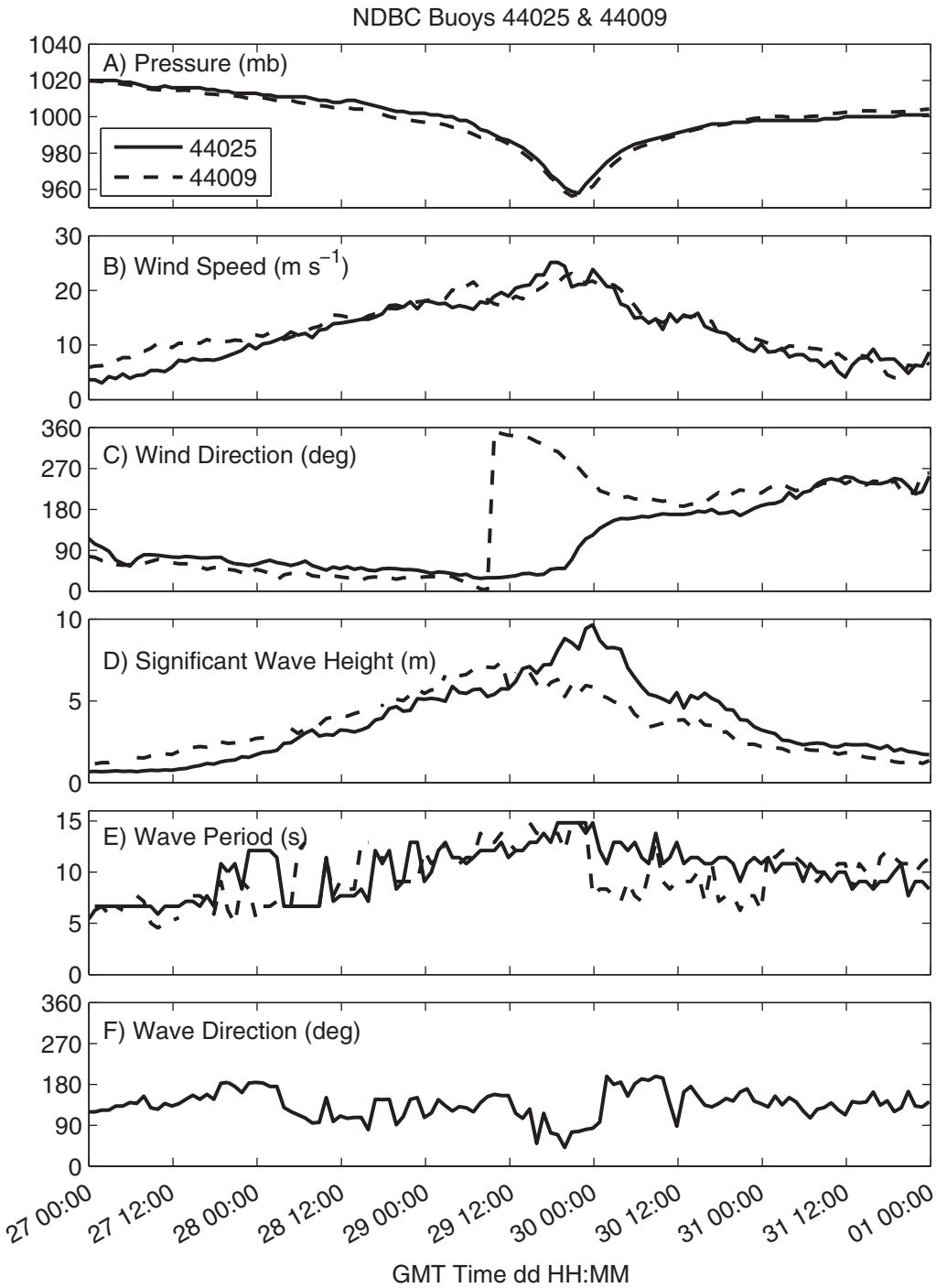

Figure 3. Buoy (solid line) 44025 and (dashed line) 44009 (a) pressure, (b) wind speed, (c) wind direction from north, (d) significant wave height, (e) wave period, and (f) wave direction from north at buoy 44025 only. The *x* axis is in days hour:minute for October 2012.

a left hand turn toward the New Jersey coastline and made landfall near Brigantine, New Jersey at 23:30 GMT (Figure 1a) [*Blake et al*., 2013]. Buoy 44025 and 44009 were located to the north and south, respectively, of the storm track as it crossed the shelf (Figure 1a). Minimum sea-level pressure at 44025 and 44009 was below 960 at both locations, and maximum wind speeds peaked over 20 m s^{-1} (Figure 3). Winds were initially downwelling favorable from the northwest at 44025 and north at 44009. Winds shifted counterclockwise to be more northeasterly at 44009 on 29 October as the storm center crossed the shelf. Winds at 44025 maintained a northwesterly direction until just prior to landfall when they shifted clockwise to be

 © 2015. The Authors.

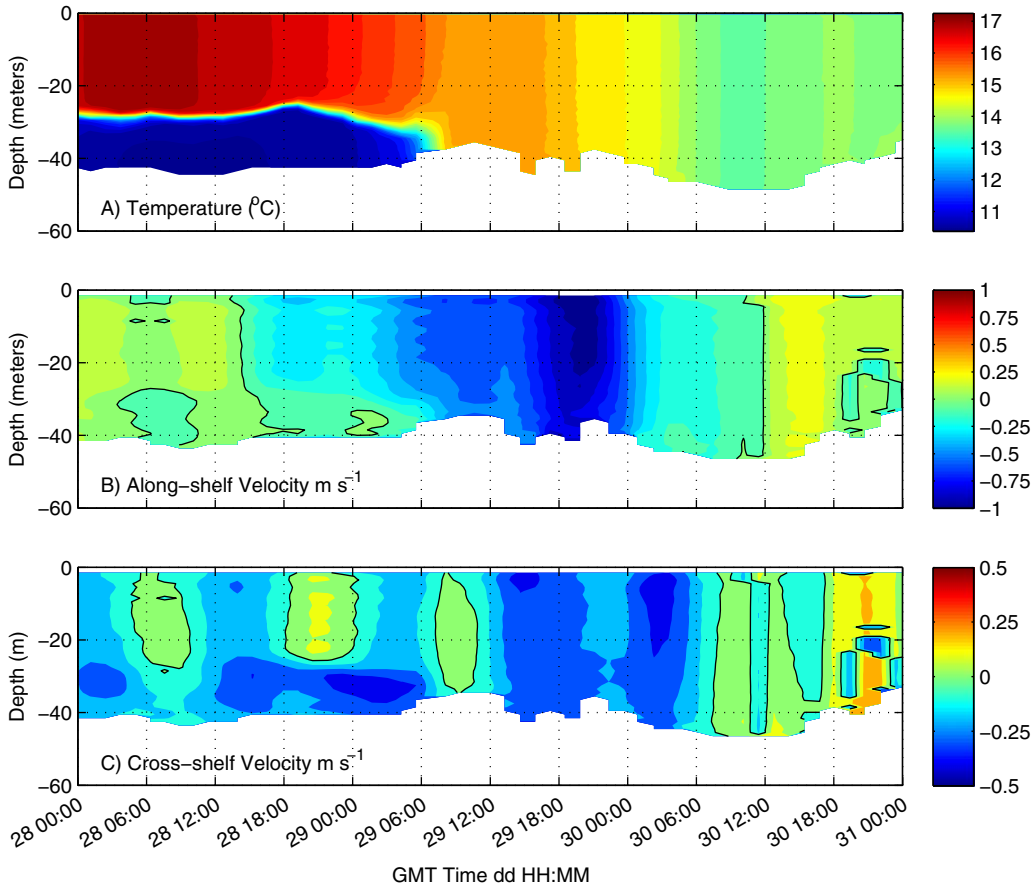

Figure 4. Cross sections along the glider track of (a) temperature, (b) along-shelf currents, and (c) cross-shelf currents with the black contour representing 0 m s^{-1}. Directions are toward and rotated 30° clockwise from north to be approximately along and cross-shelf, where positive is toward the northeast and offshore, respectively. Times on the *x* axis are as in Figure 3.

from the southwest as the eye passed between the two stations. Significant wave heights first peaked on the southern MAB at 44009 near 7 m approximately 12 h before they peaked at 44025 near 10 m. Dominant wave periods at both buoys reached 15 s near landfall. Wave periods dropped immediately following eye passage at 44009, likely due to the rapid shift in wind direction. While no wave direction data were available at 44009, mean wave direction at 44025 was generally in agreement with wind direction.

3.2. Glider Deployment

Glider RU23 was deployed on 25 October approximately 15 km off of northern New Jersey, on the southern flank of the Hudson Shelf Valley (Figure 1a). RU23 progressed southeastward in an effort to exit a coastal shipping lane prior to storm conditions. During the initial storm forcing period from 28 October at 00:00 GMT to the 29 October at 06:00 GMT, the water column observed by the glider was highly thermally stratified with surface temperatures of near 18°C and bottom temperatures as low as 10°C separated by a sharp thermocline (Figure 4a). During the stratified phase currents measured by the Nortek Aquadopp showed two-layer cross-shelf flow consistent with downwelling circulation on the shelf (Figures 4b and 4c), with offshore flow near the bottom and onshore flow near the surface. On 29 October at 06:00 GMT, the system transitioned from two to one-layer with a uniform water column temperature of ~15°C and strong alongshore flow toward the southwest. As glider horizontal speeds are on the order of 0.2–0.3 m s^{-1}, the glider was rapidly advected alongshore with the mean current until after the eye passed on 29 October at 23:30 GMT.

3.3. Model Validation

To validate the meteorological and wave forcing parameters, we calculated correlation coefficients and root-mean-square-error between modeled and observed winds, sea level pressure, wave height, and calculated bottom orbital velocities at buoy 44025 and 44009. We focused the comparison on the storm

© 2015. The Authors.

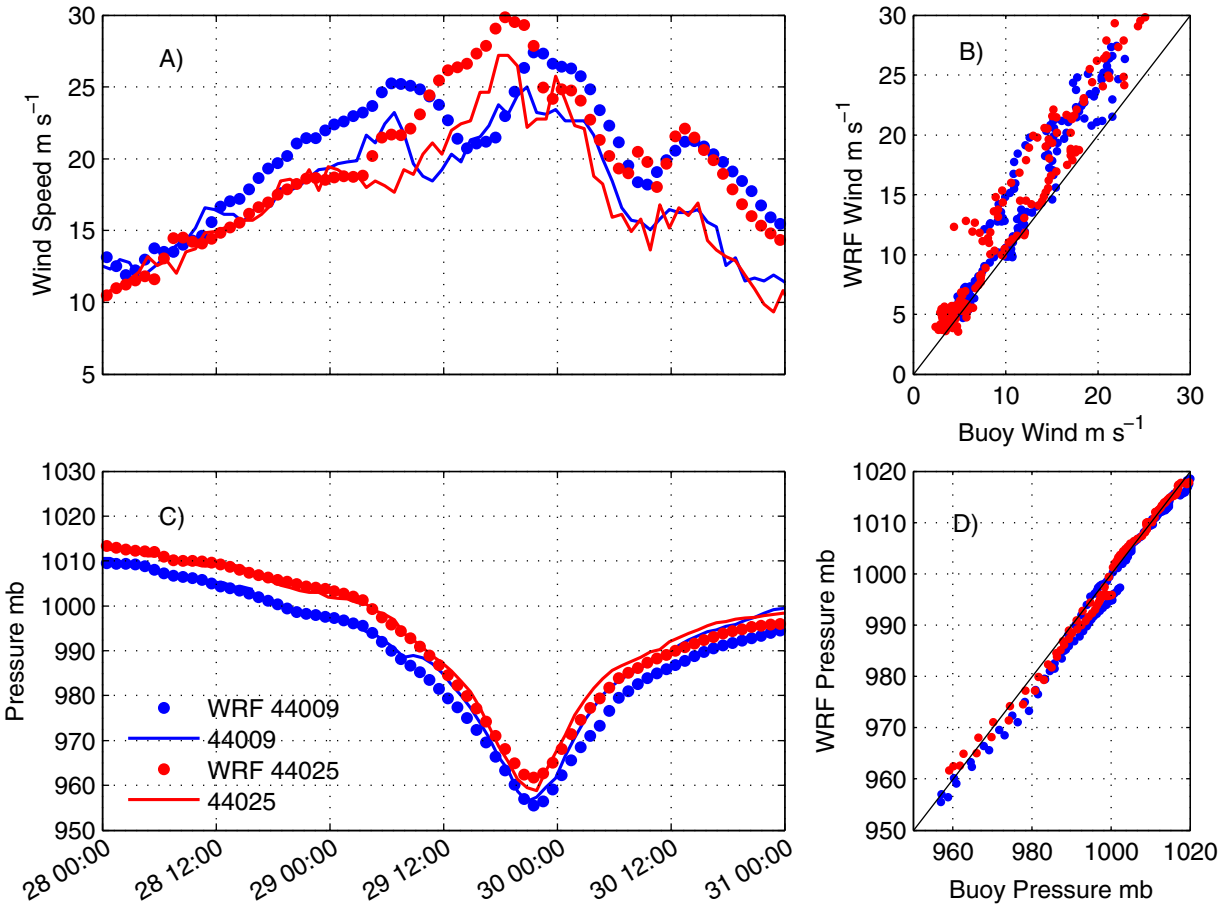

Figure 5. Comparisons of (dots) WRF and (lines) buoys (blue) 44009 and (red 44025) of (a and b) wind speed and (c and d) pressure during the storm forcing period. WRF versus buoy winds had a root mean square error (RMSE) of 4.25 and 4.14 m s^{-1} and correlation coefficients of 0.87 and 0.90 for 44009 and 44025, respectively. WRF versus buoy pressures had RMSE of 2.75 and 1.74 mb and correlation coefficients of 0.99 and 0.99 for 44009 and 44025, respectively. Time on the *x* axis is consistent with Figure 3.

forcing period between 28 October at 00:00 GMT and the 31 October at 00:00 GMT so as not to bias the validation to fair-weather conditions. Quantitative comparisons are detailed in the captions for Figures 5 and 6.

Qualitatively, the WRF hindcast wind speed and pressure (Figure 5) were in good agreement with observations at buoy 44025 and 44009. Modeled wind speeds (Figures 5a and 5b) appear to be overpredicted, likely due to WRF winds being instantaneous values extracted hourly while observed winds were hourly averages. Despite the high values, WRF winds followed along closely with the observations except for a late drop in winds at buoy 44009 on the 29 October at 12:00 GMT. Model predicted pressure was extremely close to the observations with similar trends and minimums below 960 millibars, indicating that the storm track and strength were well represented in the model.

WWIII simulated wave heights (Figures 6a and 6b) were underpredicted at both locations ahead of the storm, particularly at 44009, with peak observed wave heights occurring nearly 12 h ahead of peak modeled wave heights. Wave heights between 29 October at 12:00 GMT and 31 October at 00:00 GMT were well represented at both locations and peak modeled and observed wave heights occurred at approximately the same time at buoy 44025. Simulated bottom orbital velocities at 44025 were similarly underpredicted but generally in good agreement with the observations (Figures 6c and 6d). Differences between modeled and observed waves are likely due to the lack of spectral information included with the archived WWIII model data and coarse resolution. These properties would likely be improved by use of operational WWIII products with full spectral information or by using a modeling system such as COAWST, which includes three-way coupling between ROMS, the simulating waves near-shore (SWAN) model, and the weather research

 © 2015. The Authors.

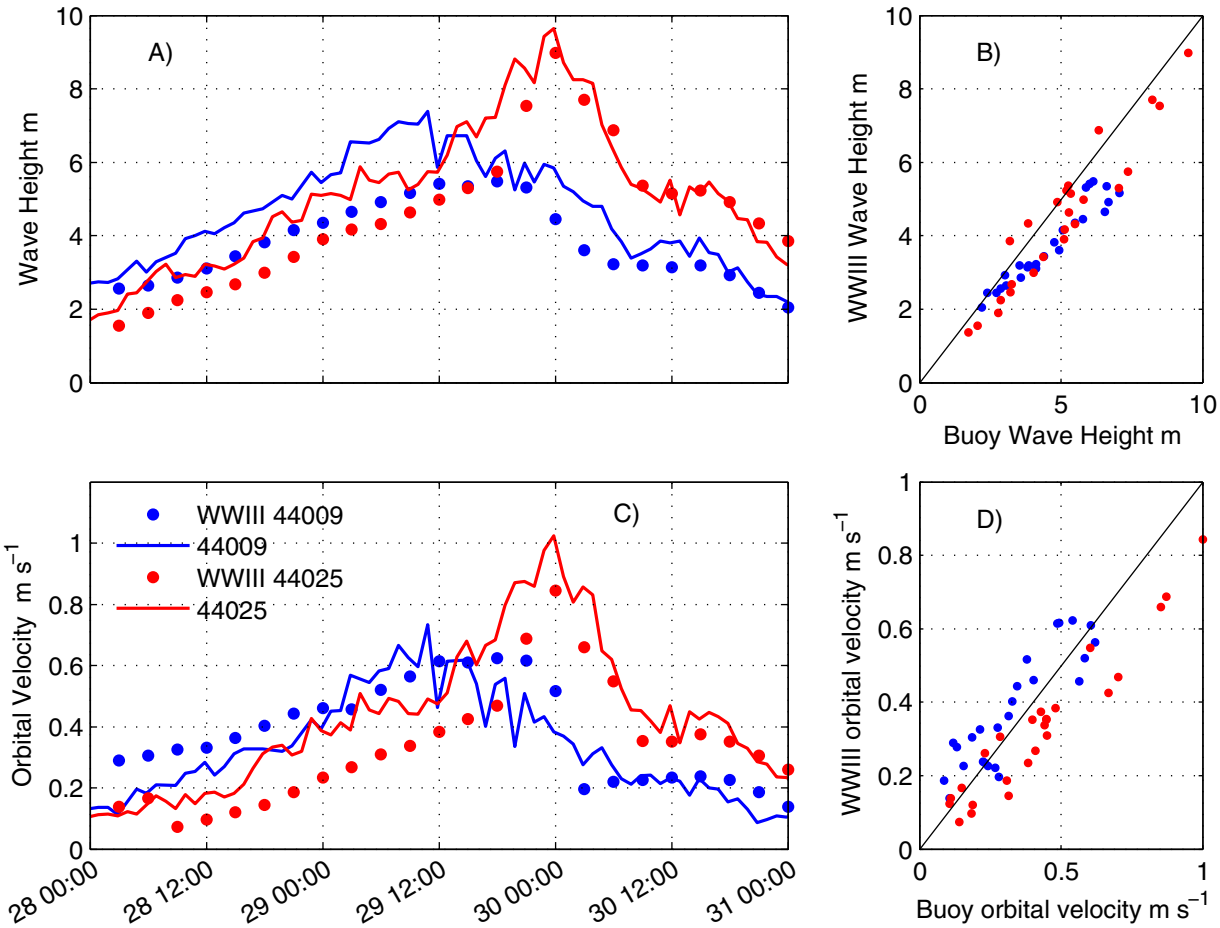

Figure 6. Comparisons of (dots) WWIII and (lines) buoys (blue) 44009 and (red 44025) of (a and b) wave height and (c and d) bottom orbital velocities during the storm. WWIII versus buoy waves had RMSE of 0.98 and 0.83 m and correlation coefficients of 0.96 and 0.95 for 44009 and 44025, respectively. WWIII versus buoy bottom orbital velocities had RMSE of 0.09 and 0.12 m s^{-1} and correlation coefficients of 0.88 and 0.96 for 44009 and 44025, respectively. Time on the *x* axis is consistent with Figure 3.

forecasting (WRF) model [*Warner et al.*, 2010]. Comparisons between the model and observations were sufficient for analysis of concurrent glider and model data north of the eye.

In order to assess modeled ESPreSSO currents, we compared depth-averaged values along the glider track to depth and time-averaged glider currents calculated using dead-reckoning [*Davis et al.*, 2003]. ESPreSSO currents were extracted hourly from the nearest grid point to each hourly glider surfacing. Both glider and ESPreSSO currents were rotated clockwise 30° from true north to align approximately alongshore and cross-shore at the glider location. ESPreSSO currents were in good agreement with the observed dead reckoned glider currents for the majority of the deployment (Figures 7a and 7b). The complex correlation coefficient between the model and glider was 0.90 with ROMS velocities rotated 8.1° counterclockwise of glider data. Cross-shore currents were generally well represented, though predicted velocities were slightly slower during the main forcing period from 29 October to at 00:00 GMT to the 30 October at 06:00 GMT. Both model predicted and observed alongshore velocities reached peak values near 1 m s^{-1} at landfall. Glider dead-reckoned currents are sensitive to accurate compass calibration. While, the compass was calibrated prior to flight and offsets from true compass direction were accounted for in postprocessing this remains a source of uncertainty in the model and observation comparisons and will require careful consideration in future deployments.

3.4. Glider and Modeled Sediment Resuspension and Transport

Typically validation of regional sediment resuspension and transport is done using poststorm surveys or using single point locations but little in situ validation over broad spatial regions and throughout the full

 © 2015. The Authors.

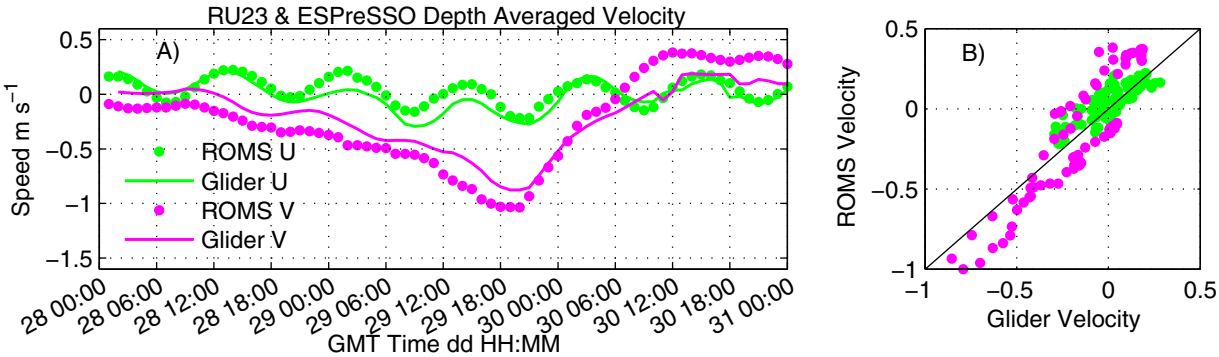

Figure 7. Comparisons of depth-averaged (dots) ROMS and (lines) glider depth-averaged currents calculated along the glider track in the (green) cross-shelf and (pink) along-shelf directions. Positive values indicate along-shelf (cross-shelf) toward the northeast (offshore). The complex correlation coefficient of ROMS versus RU23 depth-averaged currents is 0.90 with ROMS velocities rotated 8.1° counterclockwise of the glider data.

water column has previously been possible from a single set of profiling sensors. As our glider, RU23, was equipped with optical and acoustic sensors we compare along-track sediment resuspension and transport between the model and glider.

Cross sections of model suspended 0.4 and 0.1 mm sediment concentration along the glider track (Figures 8a and 8b) are compared with Aquadopp acoustic backscatter and bb3 optical backscatter (Figures 8c and 8d). Model cross sections of sediment resuspension along the glider track suggest 0.4 and 0.1 mm sediment resuspension initiate in response to storm forcing after 28 October at 12:00 GMT, with concentrations limited to within a few meters of the bed. Full water column resuspension is evident 24 h later, on the 29 October after 12:00 GMT, with large concentrations evident in the lower 10–15 m for 0.4 mm sediment, and throughout the entire water column to the surface for 0.1 mm sediment. Peak values for both grain sizes occur on the 29 October at 19:00 GMT, a few hours prior to landfall, following peak model predicted and observed wave heights and orbital velocities at buoy 44009 but prior to peak values at 44025 (Figures 5a and 5b). This is likely the timing of peak wave heights and orbital velocities at the glider location, which is approximately midway between the two buoys. Larger 0.4 mm particles fall out of suspension rapidly after the eye made landfall on 29 October at 23:30 GMT, while smaller particles had persistent elevated concentrations throughout the water column for 18 h following landfall. Acoustic backscatter (Figure 8c) was significantly different from model predicted values in two distinct ways. First, during early stages of the deployment, between 28 October at 06:00 GMT and 29 October at 00:00 GMT, there is a clear acoustic backscatter signal that fills the lower stratified (Figure 4a) region. Wave heights and orbital velocities were building during this period (Figures 6a and 6b) but were relatively weak compared to peak values. This feature was also present in optical backscatter values (Figure 8d), which indicates that the Aquadopp was likely responding to smaller fine grained sediment in the absence of a significant signal from larger grain sediments near the target 0.25 mm grain size. Cross sections of chlorophyll concentration (Figure 8e) derived from the fluorometer also suggest finer particles or biological material in this lower layer prior to transition from stratified to unstratified conditions. The second deviation from the model predicted suspended sediment is a persistent near surface acoustic backscatter signal, which peaks during peak wave and wind conditions on 29 October at 19:00 GMT. This signal is likely due to bubble entrainment in the surface boundary layer. In the lower portion of the water column acoustic backscatter qualitatively agrees with modeled 0.4 mm suspended sediment, with peak acoustic backscatter near 75 dB just prior to landfall coincident with model predicted peak concentrations. After the storm passed between 30 October at 00:00 GMT and the 31 October at 00:00 GMT, the persistent full water column acoustic backscatter near 55 dB is again likely due to fine particles that remained resuspended after coarse sand fell out of suspension. Cross sections of optical backscatter at 660 nm (Figure 8d) qualitatively agrees with concentrations of 0.1 mm sediment, which were elevated to the sea surface at nearly the same time as observed optical backscatter just prior to 29 October at 18:00 GMT, the peak in 0.1 mm concentrations and optical backscatter occurred in the model and observations similar to the acoustic and model 0.4 mm sand just prior to landfall at 19:00 GMT on 29 October. The optical signal remained high throughout the water column until 30 October near 18:00 GMT, persisting longer than modeled 0.1 mm sand. This suggests that there were likely smaller particles present than those modeled, which remained in

 © 2015. The Authors.

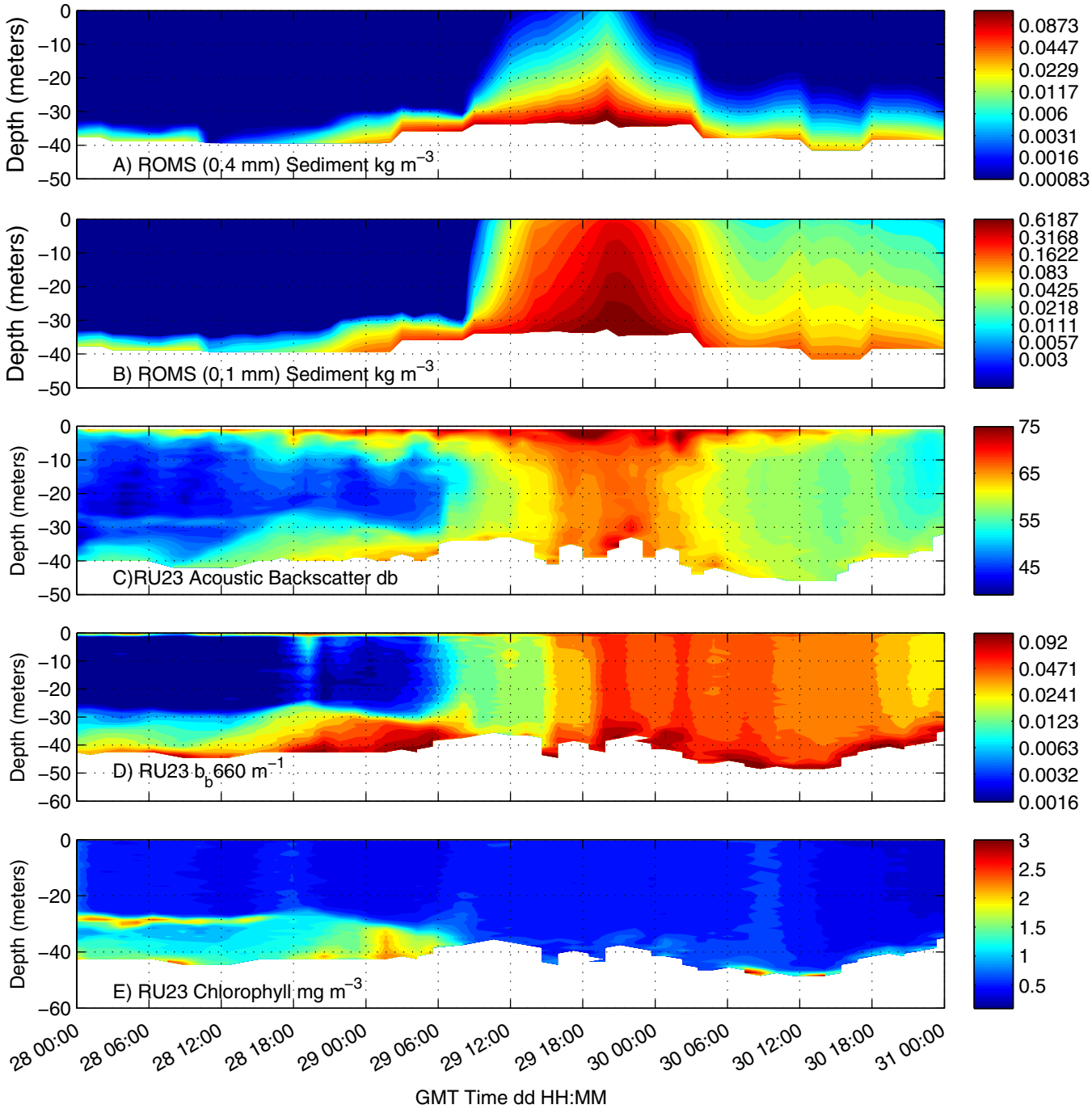

Figure 8. Cross sections of modeled sediment concentrations along the glider track for (a) 0.4 mm grain sizes, (b) 0.1 mm grain sizes and observed cross sections of (c) acoustic backscatter, (d) optical backscatter at 660 nm, and (e) chlorophyll concentration. Times along the *x* axis are as in Figure 3.

suspension well after the storm passed. Profiles extracted from each modeled, acoustic, and optical cross section (Figure 9) provide a more detailed comparison of sediment resuspension at three time periods, prior to the storm on 28 October at 06:00 GMT, just prior to landfall on 29 October at 21:00 GMT and 18 h after the storm on 30 October at 18:00 GMT. Shallow slopes were evident in modeled 0.1 and 0.4 mm grain sizes as well as acoustic and optical measurements prestorm, consistent with limited suspended sediment, though there were two features of the optical and acoustic profiles of note. The optics did not have a linear slope on a log-log scale. The subthermocline signal is likely related to organic material, detritus, chlorophyll, or other

 © 2015. The Authors.

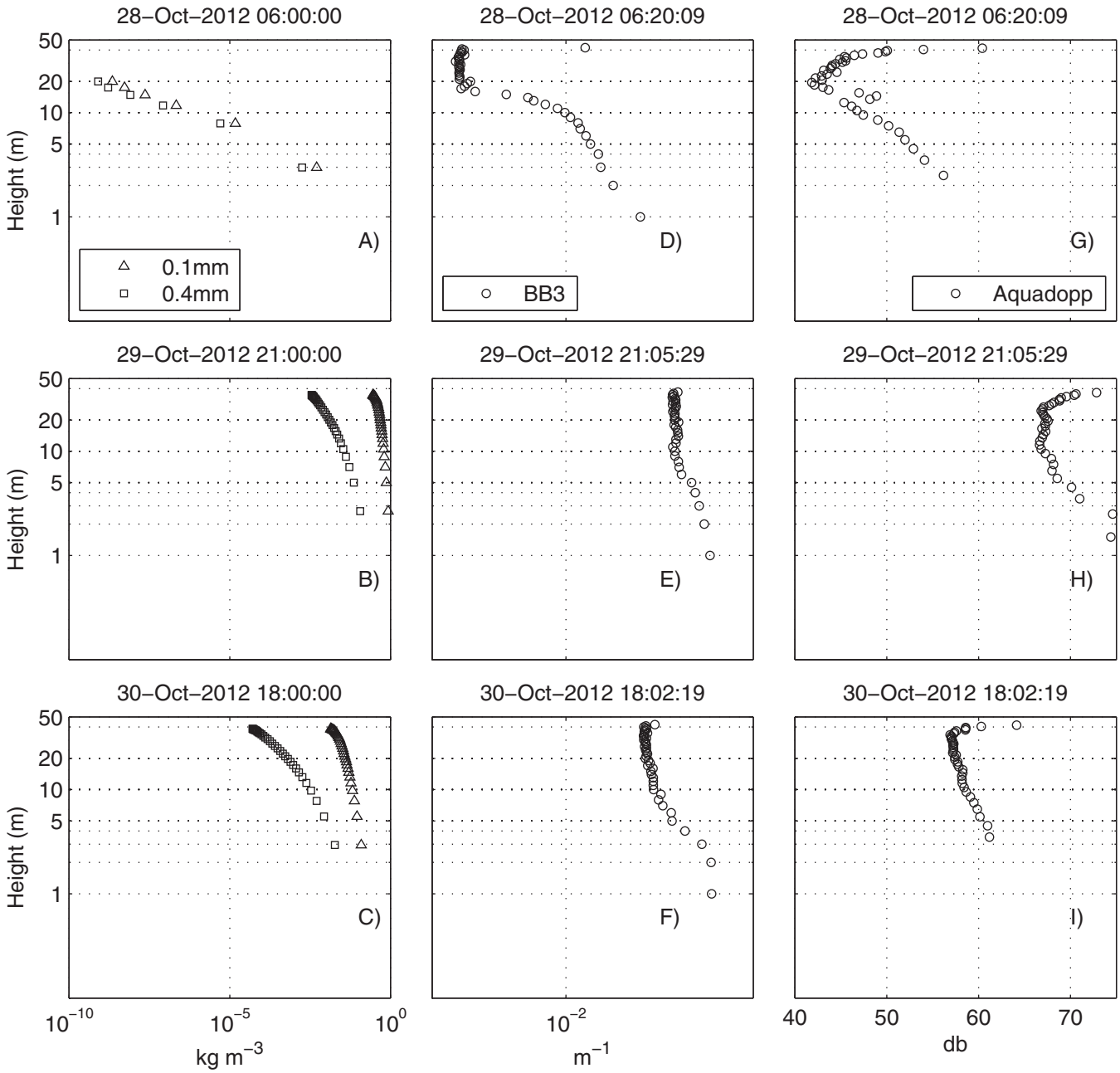

Figure 9. Log-log profiles of modeled 0.1 mm (triangles) and 0.4 mm (squares) (a–c) sediment concentration, (d–e) optical backscatter, and (g–i) semi-log profiles of acoustic backscatter. Acoustic backscatter has a logarithmic response to increased sediment concentration at the target frequency thus values are plotted on a linear db scale. Values below 10^{-10} kg m^{-3} are not plotted in Figures 9a–9c to more easily compare profiles across time points.

fine particulate matter rather than the larger cohesive sediment found on the bottom and was restricted by stratification at 20 m above the bed. Acoustics (Figure 9g) showed a positive slope above the thermocline likely due to bubbles as discussed above. During peak storm conditions model predicted and observed profiles were more vertical consistent with large concentrations of suspended sediment. Above 20 m off, the bed acoustics continued to show a positive slope likely due to bubbles and breaking waves (Figure 9h). Post-storm profiles were shallower than peak-storm but did not entirely return to prestorm conditions consistent with particles continuing to fall out of suspension.

Depth-integrated transport was calculated for modeled sediment concentrations and observed acoustic and optical backscatter. Acoustic backscatter responds logarithmically to increased observed concentration

© 2015. The Authors.

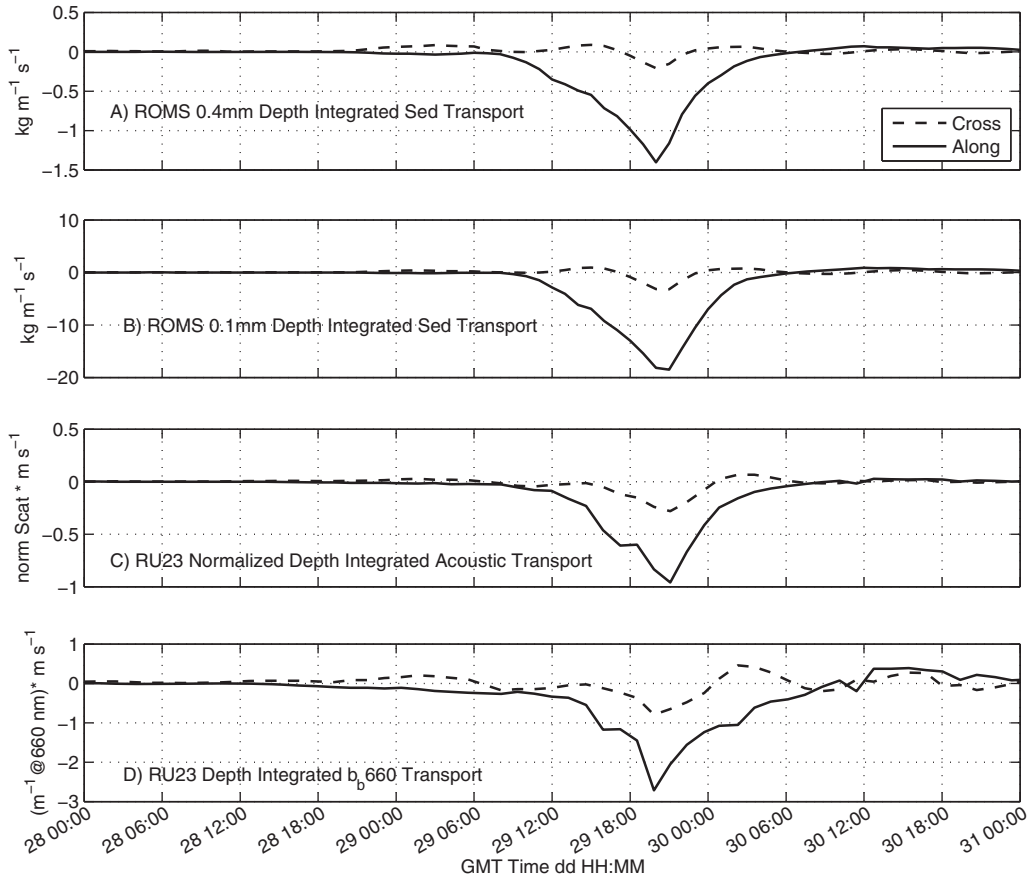

Figure 10. Depth-averaged transports calculated along the glider track for modeled (a) 0.4 mm sediment, (b) 0.1 mm sediment, (c) normalized depth-integrated acoustic transport, and depth-integrated optical backscatter transport in the (dashed) cross and (solid) along-shelf directions. Positive values indicate along-shelf (cross-shelf) toward the northeast (offshore).

[*Lohrmann*, 2001] so values were raised to the power of 10 and then normalized by dividing the maximum observed value. Additionally, acoustic backscatter shallower than 10 m were neglected from the depth integration to reduce the impact of bubble entrainment on relative transport estimates. The timing and direction of peak transport (Figure 10) were consistent between modeled and observed transports, with maximum values in the along-shelf direction on 29 October at 19:00 GMT. Inconsistency between the model predicted and observed cross-shelf currents (Figure 7) during the peak resuspension event is responsible for the limited modeled onshore transport relative to the observations on the 29 October at 19:00 GMT. The model and observations both captured the offshore cross-shelf transport immediately following landfall on 30 October at 3:00 GMT.

3.5. Regional Sediment Resuspension and Transport

Spatial maps (Figure 11) of the model predicted storm conditions over the final 12 h prior to landfall show snapshots of WRF winds (Figures 11a–11c) and WWIII waves (Figures 11d–11e) on 29 October at 12:00 GMT, 18:00 GMT and 30 October at 00:00 GMT. Winds were initially downwelling favorable and alongshore toward the southwest on the NJ shelf. WWIII model predicted wave heights were between 9 and 10 m offshore and decreased with proximity to land. As the storm approached, the coast winds shifted to a more onshore direction on the northern portion of the NJ shelf and offshore in the southern portion. Additionally, waves were near 10 m at the coastline on the northern NJ shelf, and decreased significantly to between 4 and 5 m on the southern NJ shelf as winds shifted toward the offshore direction.

As bottom orbital velocities and ambient currents are primarily responsible for sediment resuspension and transport, respectively, we present maps of the ROMS depth-averaged currents with tides retained (Figures 12a–12c) and WWIII bottom orbital velocities (Figures 12d–11f) on 29 October at 12:00 GMT, 18:00 GMT and

© 2015. The Authors.

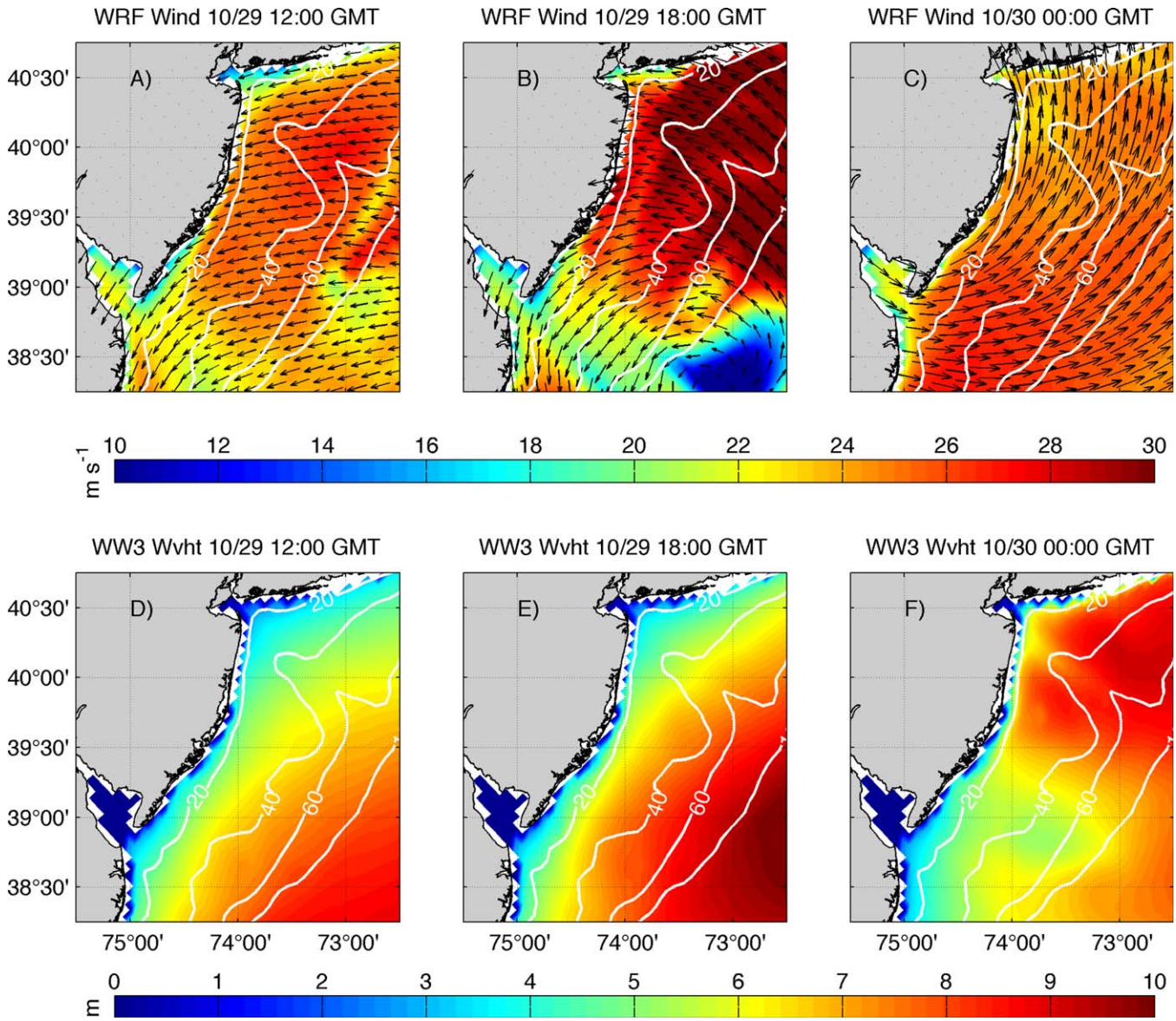

Figure 11. WRF wind on 29 October at (a) 12:00 GMT, (b) 18:00 GMT, and (c) 30 October at 00:00 GMT. WWII wave heights on 29 October at (d) 12:00 GMT, (e) 18:00 GMT, and (f) 30 October at 00:00 GMT.

30 October at 00:00 GMT. Early on 29 October, model predicted currents were highest south of the Hudson Shelf Valley and nearly uniform across the entire shelf except for a region of weak currents outside of Delaware Bay. As the storm crossed the shelf velocities were elevated to near 1 m s^{-1} across the entire domain. Current speeds were quickly reduced as the storm made landfall, likely due to the shift from alongshore winds to the southwest to weaker alongshore winds to the northeast (Figures 13a–11c). Bottom orbital velocities throughout the storm forcing duration were highest near shore south of the Hudson Shelf Valley with largest values, over 1.5 m s^{-1} near the glider deployment location on the northern side of the storm track.

Snapshots of depth-integrated suspended sediment concentration for the 0.4 mm (Figures 13a–13c) and 0.1 mm (Figures 13d–13f) are additionally mapped for the same time periods as in Figures 11 and 12 to show regional model estimates of sediment resuspension throughout the storm. On 29 October at 12:00 GMT, model predicted depth-integrated concentrations on the NJ continental shelf south of the Hudson Shelf Valley were near 1.2 and 10 kg m^{-2} for 0.4 and 0.1 mm, respectively, with highest values in the nearshore region for 0.4 mm and highest values on the central NJ shelf further offshore for the 0.1 mm

© 2015. The Authors.

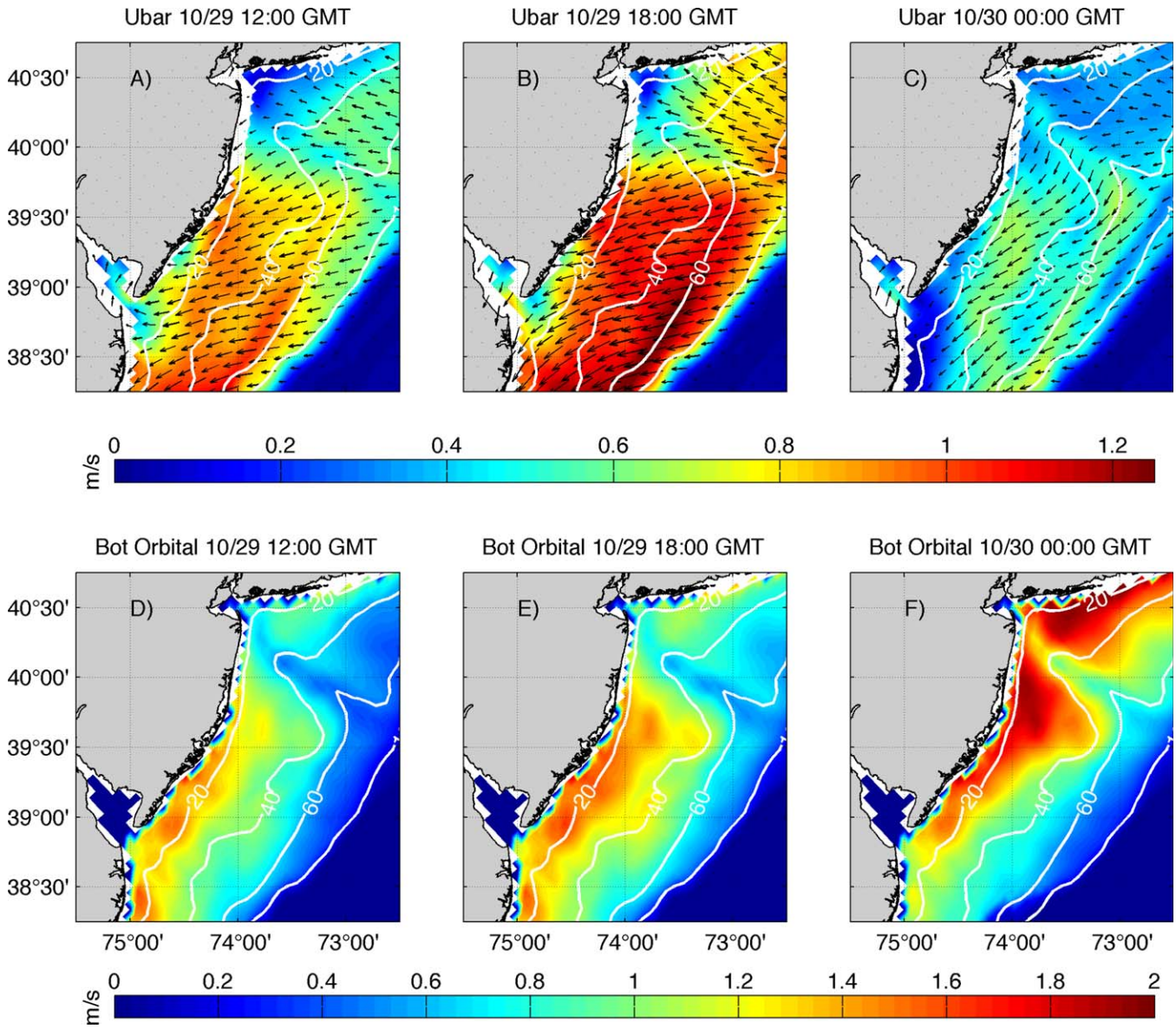

Figure 12. ROMS depth-averaged currents on 29 October at (a) 12:00 GMT, (b) 18:00 GMT, and (c) 30 October at 00:00 GMT. Bottom orbital velocities on 29 October at (d) 12:00 GMT, (e) 18:00 GMT, and (f) 30 October at 00:00 GMT.

sediment. On the 29 October at 18:00 GMT, 0.4 mm sand is resuspended along the entire inner shelf south of the Hudson Shelf Valley, while 0.1 mm sand is mobilized over the entire inner, middle, and outer shelf regions. As the storm made landfall near 30 October at 00:00 GMT, Figures 13c and 13f show that the 0.4 mm sand was resuspended coincident with peak orbital velocities (Figure 12f) and 0.1 mm sand was at a maximum across the entire northern portion of the shelf. Values for both 0.4 and 0.1 mm on the southern portion of the NJ shelf dropped significantly between 29 October at 18:00 GMT and 30 October at 00:00 GMT. This reduction was likely a result of the reduction in wave heights and orbital velocities associated with a reversal of wind direction as Sandy crossed the shelf.

Bed thickness change from the initialization to the end of the model run on 31 October at 08:00 GMT (Figure 14) predicts bed erosion of over 3 cm south of the Hudson Shelf Valley on the northern portion of the NJ shelf. This region is north of the storm track, which had highest waves, orbital velocities, and winds. Deposition of near 3 cm occurred toward the southwest in the direction of along-shelf transport (Figures 12a–12d).

© 2015. The Authors.

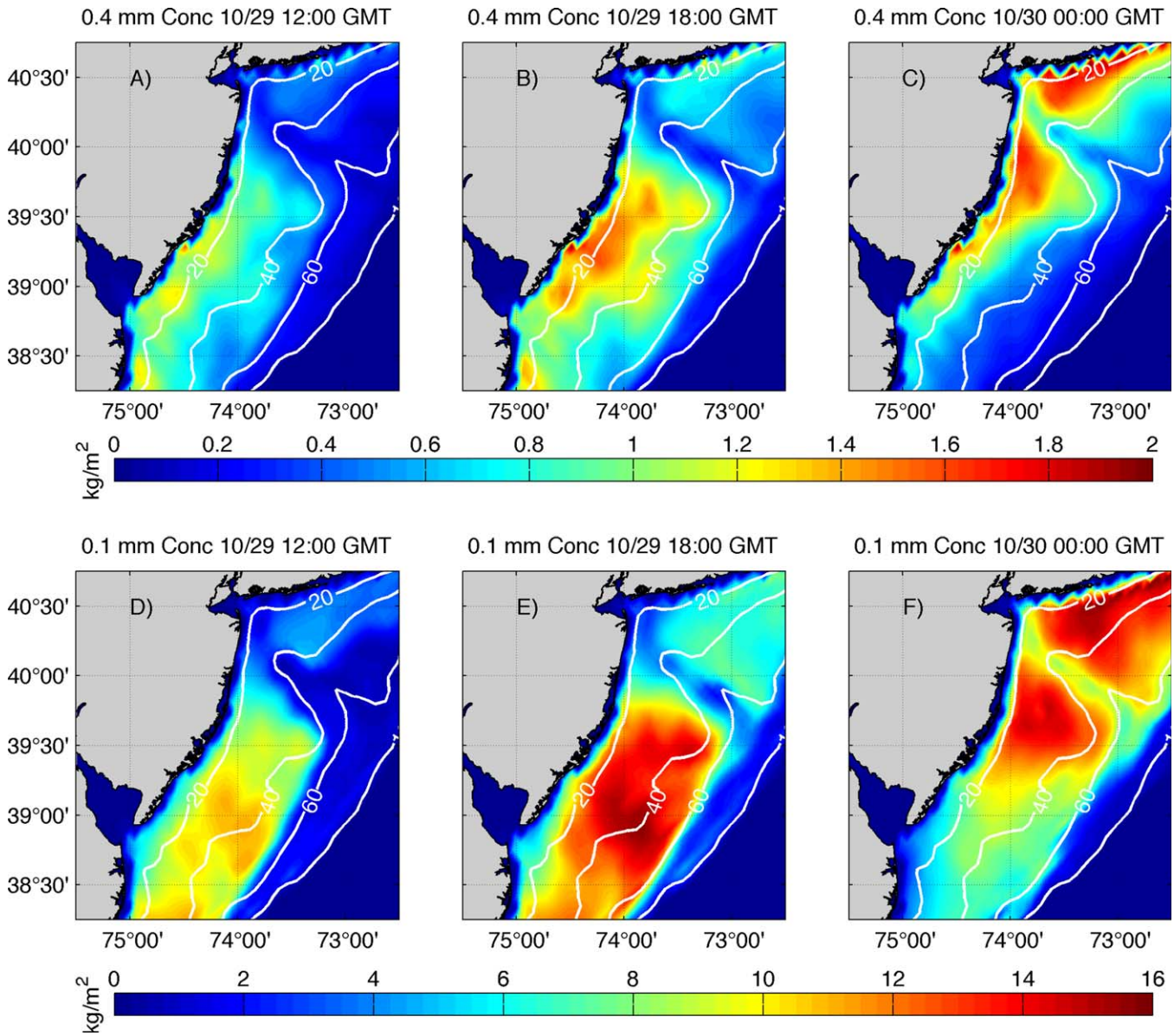

Figure 13. ROMS depth-integrated 0.4 mm sediment concentration on 29 October at (a) 12:00 GMT, (b) 18:00 GMT, and (c) 30 October at 00:00 GMT. ROMS depth-integrated 0.1 mm sediment concentration on 29 October at (d) 12:00 GMT, (e) 18:00 GMT, and (f) 30 October at 00:00 GMT.

4. Discussion

Previous studies have highlighted alongshore transport as the dominant feature of storm driven sediment transport on continental shelves [*Keen and Glenn*, 1995; *Ogston and Sternberg*, 1999; *Styles and Glenn*, 2005; *Miles et al.*, 2013], primarily during winter northeasters in the Mid-Atlantic. The typical offshore track of these storms leads to along-shelf wind stress toward the southwest and waves that increase across the entire NJ shelf [*Keim et al.*, 2004]. While Sandy initially had downwelling favorable along-shelf winds (Figures 11a and 11b), the unique cross-shelf track of the storm [*Hall and Sobel*, 2013] lead to a rotation to offshore winds on the southern portion of the NJ shelf in the 6 h before landfall. This shift on the southern NJ shelf reduced wave heights (Figures 3d and 11f), quickly reduced wave periods (Figure 3e) and ultimately reduced bottom orbital velocities (Figures 6c and 11f), which reduced bottom stress and allowed sediment that was continuing to be transported southwestward to fall out of suspension on the southern portion of the domain.

© 2015. The Authors.

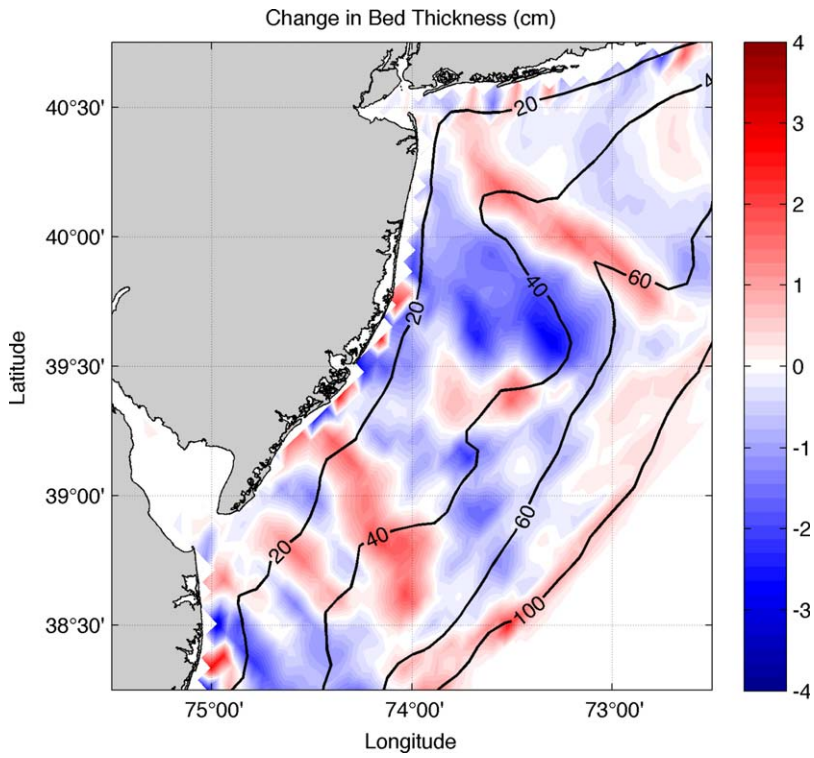

Figure 14. Change in bed thickness between the model initialization on 23 October 2012 at 00:00 GMT and 31 October at 11:00 GMT, with positive values indicating net deposition and negative values net erosion.

The modeled change in bed thickness of over + and − 3 cm on the northern and southern NJ shelf, respectively, should be approached with caution as the idealized model setup did not account for processes such as bed armoring [*Wiberg et al.*, 1994], which may have reduced available fine grained sediment for resuspension, or bedload transport, which has been shown to be orders of magnitude larger than suspended sediment transport on the continental shelf [*Styles and Glenn*, 2005]. Regardless, the in situ observations from acoustic and optical sensors mounted on Slocum glider, RU23, support model predictions and suggest that a significant portion of the bed was likely eroded from the northern NJ shelf north of the storm track and deposited along the southern portion of the shelf. This modeled erosion and deposition pattern is likely rare on the New Jersey shelf as the estimated return rate, defined as the occurrence of a sandy-like track with a category 1 or greater under constant climate conditions, is 714 years with a 95% confidence range of 435–1429 years [*Hall and Sobel*, 2013].

Autonomous underwater vehicle and ship-based surveys showed partial recovery of the bed near buoy 44009 five weeks after Hurricane Sandy made landfall [*Trembanis et al.*, 2013]. While this suggests that preservation of Sandy's sedimentary signature in the bed is not likely in the active nearshore region, the observed deposition toward the shelf break on the southern portion of the domain may be present as reworking in deeper waters is driven by more episodic wave processes [*Wiberg*, 2000].

While the onshore track, landfall, and resulting erosion and deposition patterns are likely atypical for the Mid-Atlantic, land-falling storms with onshore tracks are typical in other regions. In the Gulf of Mexico hurricanes Camille in 1969 [*Keen et al.*, 2004], Hurricane Ivan in 2004 [*Teague et al.*, 2006; *Smith et al.*, 2013; *Zambon et al.*, 2014], and Hurricanes Katrina and Rita in 2005 [*Horton et al.*, 2009]. Maximum observed scours poststorm in Hurricane Ivan were as high as 36 cm at the 60 m isobath under the region of maximum winds on the right side of the eye. Along the coast of China typhoons, such as Typhoon Morakot [*Li et al.*, 2012] also typically make landfall with an onshore track and resuspend and transport sediment. The continued development of sediment resuspension and transport models is critical to understanding coastal changes driven by land-falling storms across the world. Future studies of sediment resuspension and transport modeling and poststorm sediment analysis will benefit greatly

 © 2015. The Authors.

from a suite of observing platforms that include in situ glider data to interpret results over a broad range continental shelves.

5. Summary and Conclusions

In this study, we successfully deployed a Teledyne-Webb Slocum glider in rapid response ahead of Hurricane Sandy on the New Jersey Shelf. This mobile profiling sensor platform proved invaluable in providing in situ sediment resuspension and transport model validation, as well as simultaneous validation of currents in the hydrodynamic models. Predicted resuspension and transport suggested erosion of over 3 cm on the northern portion of the New Jersey Shelf, north of the storm track where waves and currents were highest and deposition of over 3 cm on the southern NJ shelf just north of Delaware Bay. This erosion and deposition pattern was the result of the onshore track of Hurricane Sandy, which is not typical. This study provides a valuable assessment of suspended material in a major storm using coincident acoustic and optical sensors on a glider platform, which builds confidence in the communities' ability to model regional sediment resuspension and transport. Glider technologies now have the ability to compliment invaluable high-resolution near bed measurements from moored and bottom mounted sensors. Future advances that may improve sediment concentration estimates from glider platforms include downward facing acoustic sensors, which will reduce the impact of bubble entrainment near the surface, provide data near the bed where concentrations are highest, and allow for detailed estimates of bottom-stress in situ over a large spatial area.

Acknowledgments
Glider data used in this study are available through the MARACOOS assets page http://maracoos.org/data and http://marine.rutgers.edu/cool/auvs/index.php?did=369 with more detailed data sets available upon request to tnmiles@marine.rutgers.edu. Regional Ocean Modeling System and WRF model results are also available upon request to tnmiles@marine.rutgers.edu. Buoy data and WAVEWATCH III data sets are publicly available through http://www.ndbc.noaa.gov/ and http://polar.ncep.noaa.gov/waves/index2.shtml, respectively. We are grateful for the funding support provided by NOAA grant NA11NOS0120038 as part of MARACOOS, the regional partner of U.S. IOOS and NOAA grant NA13OAR4830233 as part of CINAR, the regional partner of the CIPO. We would also like to thank Teledyne-Webb Research for providing graduate student funding, NortekUSA for providing equipment through a student equipment grant. Additionally, we would like to thank the glider technicians and pilots of the Rutgers University Center for Ocean Observing Leadership; the help of John Wilkin and the research associates of the Rutgers Ocean Modeling group with help setting up the ocean model; and commentary and help setting up the sediment model from Chris Sherwood at the United States Geological Survey (USGS).

References

Agrawal, Y. C., and H. C. Pottsmith (2000), Instruments for particle size and settling velocity observations in sediment transport, *Mar. Geol.*, *168*(1-4), 89–114, doi:10.1016/s0025-3227(00)00044-x.

Ariathurai, R., and K. Arulanandan (1978), Erosion rates of cohesive soils, *J. Hydraul. Div. Am. Soc. Civ. Eng.*, *104*(2), 279–283.

Blaas, M., C. Dong, P. Marchesiello, J. C. McWilliams, and K. D. Stolzenbach (2007), Sediment-transport modeling on Southern Californian shelves: A ROMS case study, *Cont. Shelf Res.*, *27*(6), 832–853, doi:10.1016/j.csr.2006.12.003.

Blake, E. S., T. B. Kimberlain, R. J. Berg, P. C. John, and J. L. Beven II (2013), Tropical cyclone report: Hurricane Sandy, (AL182012) 22–29 October 2012. National Hurricane Center.

Boss, E., and W. Pegau (2001), Relationship of light scattering at an angle in the backward direction to the backscattering coefficient, *Appl. Opt.*, *40*(30), 5503, doi:10.1364/AO.40.005503.

Boss, E., et al. (2009), Comparison of inherent optical properties as a surrogate for particulate matter concentration in coastal waters, *Limnol. Oceanogr. Methods*, *7*, 803–810.

Bunt, J. A. C., P. Larcombe, and C. F. Jago (1999), Quantifying the response of optical backscatter devices and transmissometers to variations in suspended particulate matter, *Cont. Shelf Res.*, *19*(9), 1199–1220, doi:10.1016/S0278–4343(99)00018-7.

Cacchione, D., and W. Grant (1987), Storm-dominated bottom boundary layer dynamics on the Northern California continental shelf: Measurements and predictions, *J. Geophys. Res.*, *92*(C2), 1817–1827.

Cahill, B., O. Schofield, R. Chant, J. Wilkin, E. Hunter, S. Glenn, and P. Bissett (2008), Dynamics of turbid buoyant plumes and the feedbacks on near-shore biogeochemistry and physics, *Geophys. Res. Lett.*, *35*, L10605, doi:10.1029/2008GL033595.

Davis, R., C. Eriksen, and C. Jones (2003), Autonomous buoyancy-driven underwater gliders, in *Technology and Applications of Autonomous Underwater Vehicles*, edited by G. Griffiths, p. 37, Taylor and Francis, London, U. K.

Drake, D. E., and D. A. Cacchione (1992), Wave-current interaction in the bottom boundary layer during storm and non-storm conditions: Observations and model predictions, *Cont. Shelf Res.*, *12*(12), 1331–1352, doi:10.1016/0278–4343(92)90058-R.

Fairall, C., and E. Bradley (1996), Bulk parameterization of air-sea fluxes for Tropical Ocean-Global Atmosphere Coupled-Ocean Atmosphere Response Experiment, *J. Geophys. Res.*, *101*(C2), 3747–3764.

Fairall, C. W., E. F. Bradley, J. E. Hare, A. A. Grachev, and J. B. Edson (2003), Bulk parameterization of air-sea fluxes: Updates and verification for the COARE algorithm, *J. Clim.*, *16*(4), 571.

Glenn, S., C. Jones, M. Twardowski, L. Bowers, J. Kerfoot, J. Kohut, D. Webb, and O. Schofield (2008), Glider observations of sediment resuspension in a Middle Atlantic Bight fall transition storm, *Limnol. Oceanogr. Methods*, *53*(5 part 2), 2180–2196, doi:10.4319/lo.2008.53.5_part_2.2180.

Glenn, S. M., and W. D. Grant (1987), A suspended sediment stratification correction for combined wave and current flows, *J. Geophys. Res.*, *92*(C8), 8244–8264.

Goff, J. A., C. J. Jenkins, and S. J. Williams (2008), Seabed mapping and characterization of sediment variability using the usSEABED data base, *Cont. Shelf Res.*, *28*(4–5), 614–633, doi:10.1016/j.csr.2007.11.011.

Grant, W., and O. Madsen (1979), Combined wave and current interaction with a rough bottom, *J. Geophys. Res.*, *84*(8), 1797–1808.

Grant, W. D., and O. S. Madsen (1986), The continental-shelf bottom boundary layer, *Annu. Rev. Fluid Mech.*, *18*(1), 265–305, doi:10.1146/annurev.fl.18.010186.001405.

Haidvogel, D. B., et al. (2008), Ocean forecasting in terrain-following coordinates: Formulation and skill assessment of the Regional Ocean Modeling System, *J. Comput. Phys.*, *227*(7), 3595–3624, doi:10.1016/j.jcp.2007.06.016.

Hall, T. M., and A. H. Sobel (2013), On the impact angle of Hurricane Sandy's New Jersey landfall, *Geophys. Res. Lett.*, *40*, 2312–2315, doi:10.1002/grl.50395.

Hapke, B. C. J., O. Brenner, R. Hehre, B. J. Reynolds, S. Jewell, and U. S. G. Survey (2013), *Coastal Change from Hurricane Sandy and the 2012-13 winter storm season, US Geological Survey Open-File Report 1231*, *37*, Fire Island, N. Y.

Harris, C., and P. Wiberg (2002), Across-shelf sediment transport: Interactions between suspended sediment and bed sediment, *J. Geophys. Res.*, *107*(C1), 3008, doi:10.1029/2000JC000634.

 © 2015. The Authors.

Harris, C. K., B. Butman, and P. Traykovski (2003), Winter-time circulation and sediment transport in the Hudson Shelf Valley, *Cont. Shelf Res.*, *23*(8), 801–820, doi:10.1016/S0278-4343(03)00025-6.

Hofmann, E., J.-N. Druon, K. Fennel, M. Friedrichs, D. Haidvogel, C. Lee, A. Mannino, C. McClain, R. Najjar, and J. O'Reilly (2008), Eastern US continental shelf carbon budget integrating models, data assimilation, and analysis, *Oceanography*, *21*(1), 86–104.

Horton, B. P., V. Rossi, and A. D. Hawkes (2009), The sedimentary record of the 2005 hurricane season from the Mississippi and Alabama coastlines, *Quat. Int.*, *195*, 15–30, doi:10.1016/j.quaint.2008.03.004.

Hu, K., P. Ding, Z. Wang, and S. Yang (2009), A 2D/3D hydrodynamic and sediment transport model for the Yangtze Estuary, China, *J. Mar. Syst.*, *77*(1–2), 114–136, doi:10.1016/j.jmarsys.2008.11.014.

Keen, T., and S. Glenn (2002), Predicting bed scour on the continental shelf during Hurricane Andrew, *J. Waterw. Port Coastal Ocean Eng.*, *128*(6), 249–257, doi:10.1061/(ASCE)0733-950X(2002)128:6(249).

Keen, T. R., and S. M. Glenn (1995), A coupled hydrodynamic-bottom boundary layer model of storm and tidal flow in the middle Atlantic Bight of North America, *J. Phys. Oceanogr.*, *25*(3), 391–406, doi:10.1175/1520-0485(1995)025<0391:ACHBLM>2.0.CO;2.

Keen, T. R., S. J. Bentley, W. C. Vaughan, and C. A. Blain (2004), The generation and preservation of multiple hurricane beds in the northern Gulf of Mexico, *Mar. Geol.*, *210*, 79–105, doi:10.1016/j.margeo.2004.05.022.

Keim, B. D., R. A. Muller, and G. W. Stone (2004), Spatial and temporal variability of coastal storms in the North Atlantic Basin, *Mar. Geol.*, *210*(1–4), 7–15, doi:10.1016/j.margeo.2003.12.006.

Li, Y., A. Wang, L. Qiao, J. Fang, and J. Chen (2012), The impact of typhoon Morakot on the modern sedimentary environment of the mud deposition center off the Zhejiang-Fujian coast, China, *Cont. Shelf Res.*, *37*, 92–100, doi:10.1016/j.csr.2012.02.020.

Lohrmann, A. (2001), Monitoring sediment concentration with acoustic backscattering instruments, *Nortek Tech. Note*, (I), 1–5.

Lynch, J. F., T. F. Gross, C. R. Sherwood, J. D. Irish, B. H. Brumley, and J. D. Irish (1997), Acoustical and optical backscatter measurements of sediment transport, Continental Shelf Research *17*(4), 337–366.

Madsen, O. (1994), Spectral wave-current bottom boundary layer flows, *Coastal Eng.*, *1*(24), 384–398.

Madsen, O., and P. Wikramanayake (1991), Simple models for turbulent wave current bottom boundary layer flow, U. S. Army Corps of Engineers, WES, Report No. DRP-91-1.

McLean, S. (1991), Depth-integrated suspended-load calculations, *J. Hydraul. Eng.*, *117*(11), 1440–1458.

Meyer-Peter, E., and R. Müller (1948), Formulas for bed-load transport, in *Proceedings of the 2nd Meeting of the International Association for Hydraulic Structures Research*, pp. 39–64.

Miles, T., S. Glenn, and O. Schofield (2013), Temporal and spatial variability in fall storm induced sediment resuspension on the Mid-Atlantic Bight, *Cont. Shelf Res.*, *63*, Supplement, S36–S49, doi:10.1016/j.csr.2012.08.006.

Ogston, A., D. Cacchione, R. Sternberg, and G. Kineke (2000), Observations of storm and river flood-driven sediment transport on the northern California continental shelf, *Cont. Shelf Res.*, *20*(16), 2141–2162, doi:10.1016/S0278-4343(00)00065-0.

Ogston, A. S., and R. W. Sternberg (1999), Sediment-transport events on the northern California continental shelf, *Mar. Geol.*, *154*, 69–82, doi:10.1016/S0025-3227(98)00104-2.

Olabarrieta, M., J. Warner, and B. Armstrong (2012), Ocean-atmosphere dynamics during Hurricane Ida and Nor'Ida: An application of the coupled ocean-atmosphere-wave-sediment transport (COAWST) modeling system, *Ocean Modell.*, *43–44*, 112–137, doi:10.1016/j.ocemod.2011.12.008.

Papanicolaou, A., and M. Elhakeem (2008), Sediment transport modeling review—Current and future developments, *J. Hydraul. Eng.*, *134*(1), 1–14.

Ruiz, S., L. Renault, B. Garau, and J. Tintoré (2012), Underwater glider observations and modeling of an abrupt mixing event in the upper ocean, *Geophys. Res. Lett.*, *39*, L01603, doi:10.1029/2011GL050078.

Schofield, O., et al. (2007), Slocum gliders: Robust and ready, *J. Field Robotics*, *24*(6), 473–485, doi:10.1002/rob.20200.

Shchepetkin, A., and J. McWilliams (2009), Computational kernel algorithms for fine-scale, multi-process, long-time oceanic simulations, *Comput. Methods*, *14*(8), 121–183, doi:10.1016/S1570-8659(08)01202-0.

Shchepetkin, A. F., and J. C. McWilliams (2005), The regional oceanic modeling system (ROMS): A split-explicit, free-surface, topography-following-coordinate oceanic model, *Ocean Modell.*, *9*(4), 347–404, doi:10.1016/j.ocemod.2004.08.002.

Sherwood, C. R., B. Butman, D. A. Cacchione, D. E. Drake, T. F. Gross, R. W. Sternberg, P. L. Wiberg, and A. J. Williams (1994), Sediment-transport events on the northern California continental shelf during the 1990–1991 STRESS experiment, *Cont. Shelf Res.*, *14*(10–11), 1063–1099, doi:10.1016/0278-4343(94)90029-9.

Skamarock, W., J. Klemp, J. Dudhia, D. O. Gill, D. M. Barker, M. G. Duda, X.-Y. Huang, W. Wang, and J. G. Powers (2008), A description of the advanced research WRF version 3, *NCAR Tech. Note NCAR/TN-475+STR*.

Smith, T. A., S. Chen, T. Campbell, P. Martin, W. E. Rogers, S. Gaberšek, D. Wang, S. Carroll, and R. Allard (2013), Ocean-wave coupled modeling in COAMPS-TC: A study of Hurricane Ivan (2004), *Ocean Modell.*, *69*, 181–194, doi:10.1016/j.ocemod.2013.06.003.

Soulsby, R. L., and J. S. Damgaard (2005), Bedload sediment transport in coastal waters, *Coastal Eng.*, *52*(8), 673–689, doi:10.1016/j.coastaleng.2005.04.003.

Styles, R., and S. Glenn (2000), Modeling stratified wave and current bottom boundary layers on the continental shelf, *J. Geophys. Res.*, *105*(C10), 24,119–24,139.

Styles, R., and S. Glenn (2002), An Optimized Combined Wave and Current Algorithm for Arbitrary Bed Roughness, Technical Report, Coastal Phys. Oceanogr. Lab, Dep. of Geol. Sci., Univ. of S. C., Columbia, S. C.

Styles, R., and S. M. Glenn (2005), Long-term sediment mobilization at a sandy inner shelf, *J. Geophys. Res.*, *110*, C04S90, doi:10.1029/2003JC002175.

Teague, W. J., E. Jarosz, T. R. Keen, D. W. Wang, and M. S. Hulbert (2006), Bottom scour observed under Hurricane Ivan, *Geophys. Res. Lett.*, *33*, L07607, doi:10.1029/2005GL025281.

Thorne, P. D., and D. M. Hanes (2002), A review of acoustic measurement of small-scale sediment processes, *Cont. Shelf Res.*, *22*(4), 603–632, doi:10.1016/S0278-4343(01)00101-7.

Todd, R. E., D. L. Rudnick, M. R. Mazloff, R. E. Davis, and B. D. Cornuelle (2011a), Poleward flows in the southern California Current System: Glider observations and numerical simulation, *J. Geophys. Res.*, *116*, C02026, doi:10.1029/2010JC006536.

Todd, R. E., D. L. Rudnick, R. E. Davis, and M. D. Ohman (2011b), Underwater gliders reveal rapid arrival of El Niño effects off California's coast, *Geophys. Res. Lett.*, *38*, L03609, doi:10.1029/2010GL046376.

Trembanis, A., C. DuVal, J. Beaudoin, V. Schmidt, D. Miller, and L. Mayer (2013), A detailed seabed signature from Hurricane Sandy revealed in bedforms and scour, *Geochem. Geophys. Geosyst.*, *14*, 4334–4340, doi:10.1002/ggge.20260.

Trowbridge, J. H., and A. R. M. Nowell (1994), An introduction to the Sediment TRansport Events on Shelves and Slopes (STRESS) program, *Cont. Shelf Res.*, *14*(10–11), 1057–1061, doi:10.1016/0278-4343(94)90028-0.

 © 2015. The Authors.

Visbeck, M. (2002), Deep velocity profiling useding lowered acoustic Doppler current profilers: Bottom track and inverse solutions, *J. Atmos. Oceanic Technol.*, *19*, 794–807.

Warner, J., B. Butman, and P. Dalyander (2008a), Storm-driven sediment transport in Massachusetts Bay, *Cont. Shelf Res.*, *28*(2), 257–282, doi:10.1016/j.csr.2007.08.008.

Warner, J. C., C. R. Sherwood, R. P. Signell, C. K. Harris, and H. G. Arango (2008b), Development of a three-dimensional, regional, coupled wave, current, and sediment-transport model, *Comput. Geosci.*, *34*(10), 1284–1306, doi:10.1016/j.cageo.2008.02.012.

Warner, J. C., B. Armstrong, R. He, and J. B. Zambon (2010), Development of a Coupled Ocean-Atmosphere-Wave-Sediment Transport (COAWST) modeling system, *Ocean Modell.*, *35*(3), 230–244, doi:10.1016/j.ocemod.2010.07.010.

Wiberg, P. (2000), A perfect storm: Formation and potential for preservation of storm beds on the continental shelf, *Oceanography*, *13*(3), 93–99, doi:10.5670/oceanog.2000.18.

Wiberg, P. L., and C. K. Harris (1994), Ripple geometry in wave-dominated environments, *J. Geophys. Res.*, *99*(C1), 775–789.

Wiberg, P. L., and C. R. Sherwood (2008), Calculating wave-generated bottom orbital velocities from surface-wave parameters, *Comput. Geosci.*, *34*(10), 1243–1262, doi:10.1016/j.cageo.2008.02.010.

Wiberg, P. L., D. E. Drake, and D. A. Cacchione (1994), Sediment resuspension and bed armoring during high bottom stress events on the northern California inner continental shelf: Measurements and predictions, *Cont. Shelf Res.*, *14*(10–11), 1191–1219, doi:10.1016/0278–4343(94)90034-5.

Wilkin, J., and E. Hunter (2013), An assessment of the skill of real-time models of Mid-Atlantic Bight continental shelf circulation, *J. Geophys. Res. Oceans*, *118*, 2919–2933, doi:10.1002/jgrc.20223.

Xu, Y., B. Cahill, J. Wilkin, and O. Schofield (2013), Role of wind in regulating phytoplankton blooms on the Mid-Atlantic Bight, *Cont. Shelf Res.*, *63* Supplement, S26–S35, doi:10.1016/j.csr.2012.09.011.

Zambon, J. B., R. He, and J. C. Warner (2014), Investigation of hurricane Ivan using the coupled ocean-atmosphere-wave-sediment transport (COAWST) model, *Ocean Dyn.*, *64*(11), 1535–1554, doi:10.1007/s10236-014-0777-7.

Zhang, W. G., J. L. Wilkin, J. C. Levin, and H. G. Arango (2009), An adjoint sensitivity study of buoyancy- and wind-driven circulation on the New Jersey inner shelf, *J. Phys. Oceanogr.*, *39*(7), 1652–1668, doi:10.1175/2009JPO4050.1.

 © 2015. The Authors.